Monitoring of Post-Outburst Near-Infrared Flux from the Anomalous X-ray Pulsar 1E 2259+586

Cindy R. Tam

Department of Physics
McGill University
Montreal, QC
H3A 2T8
Canada

A thesis submitted to McGill University in partial fulfilment of the requirements of the degree of Masters of Science

December 14, 2004

Your file Votre référence
ISBN: 0-494-12551-9
Our file Notre référence
ISBN: 0-494-12551-9

Abstract

On 18 June 2002, the anomalous X-ray pulsar 1E 2259+586 underwent a major X-ray outburst that lasted several hours and consequently linked AXPs to the class of magnetar-candidates known as soft gamma repeaters (SGRs). Three days after the outburst, observations with the Gemini Observatory showed a near-infrared flux enhancement, presumably associated with the X-ray activity. We have since performed a $\sim$1.5 year monitoring program of the K_s band (2.15 μm) photometry, and find that the flux decreased continually, reaching its pre-burst level after about one year. Comparing both the near-IR flux increase and subsequent decay to those of the X-ray afterglow, we find them to be remarkably consistent. This correlated post-burst activity confirms the association between the X-ray outburst and IR enhancement, and implies a physical link between their origins. In the context of the magnetar model, both types of emission appear to be from the neutron star magnetosphere, although the mechanism powering IR radiation is still unclear. We also compare our results to recent optical/IR observations of other AXPs.

Résumé

Le 18 juin 2002, le pulsar 1E 2259+586, qui fait partie de la classe des "anomalous X-ray pulsars" (AXPs), a connu un sursaut majeur de rayons-X qui a duré sur plusieur heures. Cet évenement a ainsi permis d'associer les AXPs à une classe d'objets connu sous le nom de "soft gamma repeaters" (SGRs) qu'on présume être des magnetars. Trois jours après le sursaut, des observations effectuées avec le telescope Gemini ont permis de constater une augmentation du flux dans l'infrarouge proche qui serait probablement reliée à l'activité en rayons-X. Au cours des 1.5 années écoulées depuis, nous avons réalisé un suivi photométrique de la source dans la bande infrarouge K_s (2.15 μm) qui a démontré que le flux a constamment diminué pour atteindre, un an après le sursant, son niveau d'origine. L'augmentation du flux dans l'IR proche et sa diminution subséquente est en remarquable accord avec celle de la postluminescence en rayons-X. Cette correlation dans l'activité post-sursaut confirme l'association entre le sursaut de rayons-X et l'accroissement du flux IR et implique qu'un lien physique relie leur origine. Dans le cadre du modèle des magnetars, les deux types d'émission seraient issus de la magnétosphere de l'étoile à neutrons; bien que le mécanisme responsable de la contrepartie IR soit encore mal connu. Nous comparons également nos résultats avec des observations récentes en optique/IR provenant d'autres AXPs.

Acknowledgements

Many thanks to Vicky for taking me on first as a research assistant and then as a graduate student, and giving me the opportunity to gain much valuable research experience: without her guidance, this work would not have been possible. In fact, I wish to thank the entire Pulsar Group (past members included) for making my work environment such a great one, I can't imagine a better and more entertaining group of people to work with. In particular, I'd like to thank my ever-present officemates Jason and Fotis, whose help and unceasing commentary (science and otherwise-related) were key to my scholastic success. Here in the department, there are many excellent friends and dining companions to acknowledge, they are (in alphabetical order): Alex, John, Maggie, Mallory, Marjorie, René, Rim, Sheila, & Thomas. Special thanks to Aaron for his constant support at school and at home. Finally, I am extremely grateful to my mom, dad, sister and brother, who are always supportive and pretend to find what I do interesting, even when it isn't.

This work was based on observations obtained at the Gemini Observatory, which is operated by the Association of Universities for Research in Astronomy, Inc., under a cooperative agreement with the NSF on behalf of the Gemini partnership. It was also supported by NSERC Discovery Grant 228738-03, NSERC Steacie Supplement 268264-03, a CFI New Opportunities Grant, and FQRNT Team and Centre Grants.

Contents

1 Introduction **1**

1.1 Pulsars . . . 1

1.2 Anomalous X-ray Pulsars . . . 3

1.2.1 SGR-like X-ray Bursts . . . 4

1.2.2 Optical/IR Properties . . . 8

1.3 Models of Emission for AXPs . . . 8

1.3.1 Magnetar Model . . . 9

1.3.2 Accretion Disk Model . . . 12

1.4 1E 2259+586: An Overview . . . 15

2 The Gemini Observatory **17**

2.1 Telescope and Site Information . . . 17

2.2 Instrumentation . . . 19

2.2.1 NIRI . . . 19

2.2.2 Wavefront sensing . . . 21

3 IRAF Software **25**

3.1 Data Reduction . . . 25

3.1.1 Bias and Dark Current . . . 26

3.1.2 Flat Fields and Bad Pixels . . . 26

3.2 Photometry . . . 27

3.2.1 Initializing the Software 28
3.2.2 Determining the PSF 29
3.2.3 Profile Fitting 30
3.2.4 Improving the PSF Model 30
3.3 Calibration 31

4 Data Analysis **33**
4.1 Observations 33
4.2 Performing the Data Reduction 34
4.3 Photometry Calibration 36
4.4 Estimating the Uncertainties 38
4.5 Absorption Correction 39
4.6 Converting to Flux 39

5 Results **41**
5.1 Power-law model 42
5.2 Excess function model 45

6 Discussion **47**
6.1 Accretion Disk vs. Magnetar Model 47
6.2 Possible Sources of IR Emission 48
6.3 Constraining the Magnetar Model 50
6.4 IR Variability in Other AXPs 51

7 Conclusions **53**

List of Figures

1.1 Pulsar $P - \dot{P}$ diagram 5
1.2 *RXTE* light curve 7
1.3 Broadband emission spectrum 16

2.1 Diagram of the Gemini telescope 18
2.2 Ray trace of the f/6 camera 22
2.3 Near-IR detector response uniformity 23
2.4 Gemini near-IR filters 24

4.1 Image reduction process 36
4.2 Final Gemini K_s band images 37

5.1 X-ray and near-IR flux decay curve 46

List of Tables

1.1 Properties of AXPs 6

4.1 Near-IR observing parameters 34

4.2 K_s band photometry results 40

5.1 *RXTE* X-ray data 43

5.2 Results of power-law and excess function fitting 44

Preface

Contribution of Authors

This work was originally presented in the following journal article by myself and three co-authors: *Correlated Infrared and X-ray Flux Changes Following the 2002 June Outburst of the Anomalous X-ray Pulsar 1E 2259+586*, Cindy R. Tam[1], Victoria M. Kaspi[1], Marten H. van Kerkwijk[2] & Martin Durant[2] 2004, ApJ, 617, L53.

M. Durant assisted with the data reduction and photometry.

M. H. van Kerkwijk helped analyse and interpret the data.

V. M. Kaspi initiated the project by proposing for and receiving ToO and subsequent observations at the Gemini Observatory, and contributed substantially in the analysis and interpretation of the data.

[1]Department of Physics, Ernest Rutherford Building, McGill University, 3600 University Street, Montreal, QC, H3A 2T8, Canada

[2]Department of Astronomy & Astrophysics, University of Toronto, 60 Saint George Street, Toronto, ON, M5T 1P4, Canada

Chapter 1

Introduction

1.1 Pulsars

Neutron stars, the dense stellar remnants left behind after a supernova explosion, come in many flavours. One of the more exotic classes of neutron stars, if not astronomical objects in general, are pulsars: rapidly rotating neutron stars possessing strong magnetic fields, with rotational spin and magnetic field axes misaligned. By far, the most common of these are "rotation-powered" pulsars, which emit electromagnetic radiation at the frequency of the spinning magnetic dipole. They are typically, though not exclusively, observed at radio wavelengths, and have spin periods of $P \sim 0.1 - 10$ s and spin-down rates of $\dot{P} \sim 10^{-12} - 10^{-17}$. The total luminosity available is defined by the loss of rotational kinetic energy:

$$E = \frac{1}{2} I \omega^2 = \frac{2\pi^2 I}{P^2} \tag{1.1}$$

$$\dot{E} = \frac{dE}{dt} = -\frac{4\pi^2 I \dot{P}}{P^3} \tag{1.2}$$

where I is the moment of inertia, usually approximated as $\frac{2}{5}MR^2 \approx 10^{45}$ g cm^2, and $\omega = 2\pi/P$. If a pulsar's geometry is simplified to that of a braking magnetic dipole in a vacuum, the surface magnetic field at the equator can be described by

$$B_s \approx \left(\frac{3Ic^3 P\dot{P}}{8\pi^2 R^6}\right)^{1/2} \tag{1.3}$$

which gives $B_s \approx 3.2 \times 10^{19}(P\dot{P})^{1/2}$ G, assuming the radius $R = 10^6$ cm (Manchester & Taylor, 1977, Chapter 9); typically, $B_s \sim 10^{12}$ G. The "characteristic", or spin-down, age of a pulsar can also be approximated simply in terms of P and $\dot{P}$:

$$\tau_c = \frac{P}{2\dot{P}} \tag{1.4}$$

if the pulsar's initial rotation period P_0 is assumed to be negligible compared to its current P.

A pulsar is referred to as "accretion-powered" if it has either a binary stellar companion or a companion disk formed from residual stellar matter, from which it accretes material. In low-mass X-ray binary (LMXB) systems, the companion overflows its Roche lobe, sending matter spiraling towards the pulsar through an accretion disk, which transfers angular momentum to the pulsar and causes it to spin up (Manchester & Taylor, 1977, Chapter 5). High-mass X-ray binaries (HMXBs) transfer matter through either a high-velocity stellar wind, or atmospheric Roche-lobe overflow (Tauris & van den Heuvel, 2004). Radiation predominantly in the form of X-ray emission is produced at the rate of potential energy lost by the infalling accreting matter:

$$L_X \approx \frac{GM\dot{M}}{R} \tag{1.5}$$

where M and R are the pulsar mass and radius, respectively, and $\dot{M}$ is the rate of mass transfer between the binary objects (Manchester & Taylor, 1977). In accreting systems, pulsation periods as high as $P \sim 1000$ s have been detected: such slow periods are achieved through the same gradual spin-down processes affecting rotation-powered pulsars, over long timescales (on the order of 10–100 Myr). Compared to rotation-powered pulsars, the number of pulsars in binary systems currently undergoing accretion is small. The stellar companion is usually a low-mass late-type main sequence star or a white dwarf in the case of LMXBs, and a high-mass OB main sequence star in HMXBs. Observationally, accretion-powered pulsars can be distinguished from isolated pulsars by evidence of orbital Doppler shifts in the pulse timing, a negative $\dot{P}$ indicating spin-up rather than spin-down, and optical detection of the secondary companion.

Rotation-powered pulsars that have been "recycled", or spun-up by accretion from a binary companion in the past, can have spin periods as short as milliseconds: these "millisecond pulsars" are spinning down, now that the accretion mechanism that originally fueled their spin up has ceased. Millisecond pulsars are often found in binary systems. Typical spin periods are in the range of $P \sim 1.6 - 10$ ms, and $\dot{P}$ values are on average low, from $10^{-19} - 10^{-21}$; they are inferred to be much older ($\tau_c \sim 10^9 - 10^{10}$ yr) than the more common, slower rotation-powered pulsars.

1.2 Anomalous X-ray Pulsars

Within the pulsar class, there exists another subgenre of objects known as "anomalous X-ray pulsars", named so because of the long-standing mystery surrounding the nature of their power source (see Kaspi & Gavriil, 2004, for a recent review). The observed X-ray luminosities of the six confirmed AXPs, based on best distance estimates, appear to be too large to be accounted for by rotational spin-down alone, nor do they show any evidence of binary accretion; thus, it appears that AXPs are isolated neutron stars whose X-ray emission is powered by some unique mechanism. Table 1.1 contains a summary of typical AXP properties.

The observed spin properties of the six known (XTE J1810−197, 1E 1048.1−5937, 1E 2259+586, 4U 0142+61, 1RXS J170849−400910, and 1E 1841−045) and two candidate (AX J1845.0−0258 and CXOU 010043.1−721134) AXPs generally fall within a narrow range of values. They are rotating slower ($P = 5 - 12$ s) and spinning down faster ($\dot{P} \sim 10^{-11} - 10^{-13}$) than most other pulsars (see Figure 1.1); as a result, their inferred surface magnetic fields are uncommonly high ($B_s \sim 10^{14} - 10^{15}$ G from equation 1.3). Low characteristic ages and two associations with supernova remnants (SNRs) imply that these are relatively young objects. All are located within the Galactic plane, though their distances have not yet been well established. Their X-ray spectra are usually well described as consisting of two components: a thermal blackbody ($kT \approx 0.4 - 0.7$ keV) with a power-law tail ($\Gamma \approx 2 - 5$).

1.2.1 SGR-like X-ray Bursts

Three AXPs have exhibited X-ray flux variability in the form of bursts. The first example was from the "noisy" rotator 1E 1048.1−5937: two short, faint bursts separated by two weeks were discovered with the *Rossi X-ray Timing Explorer* (*RXTE*) Proportional Counter Array (PCA) by Gavriil et al. (2002) in late 2001, and very recently another single burst was detected (Kaspi et al., 2004). Individual bursts are spikes in X-ray brightness, often several orders of magnitude brighter than the flux during quiescence, that appear suddenly and fade quickly, lasting ~0.1 s or less.

This type of behavior had previously been detected in another class of objects known as "soft gamma repeaters", or SGRs (see Woods & Thompson, 2004, for a recent review); however, it wasn't until a second AXP bursting event took place that the association between the two classes became undeni-

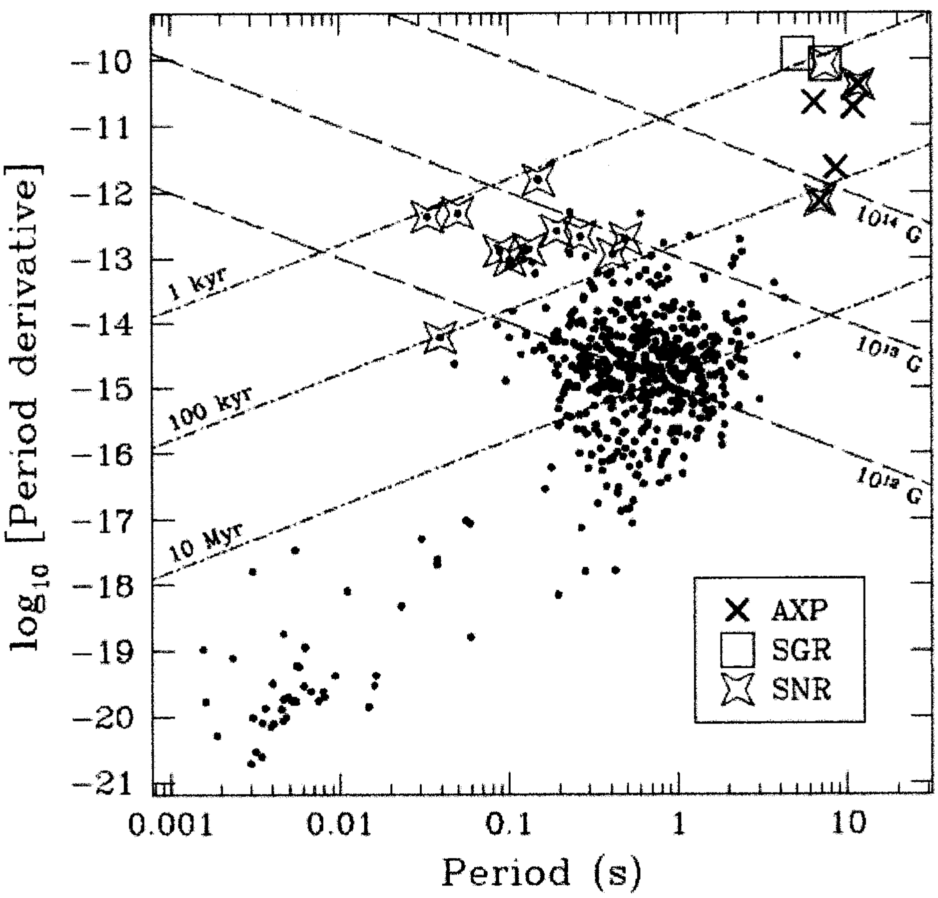

Figure 1.1: Log-log period vs. period derivative diagram of known pulsars. The "normal" rotation-powered pulsars are shown as dots near the center of the plot; millisecond pulsars are in the lower-left region. AXPs are indicated by crosses in the upper right region, with the SGRs in boxes nearby. Pulsars with supernova counterparts are marked by stars. Lines of constant magnetic field and characteristic age are indicated by dashed and dot-dashed lines, respectively.

Table 1.1: Properties of anomalous X-ray pulsars (Kaspi & Gavriil, 2004).

AXP	P (s)	$\dot{P}$ 10^{-11} (s/s)	$\dot{E}$ 10^{32} (erg/s)	L_X 10^{35} (erg/s)	B_s 10^{14} (G)	τ_c (kyr)	**SNR association**	**Absorbed K_s range** (mag)	**Ref.**[a]
XTE J1810−197[b]	5.54	1.15	26	16	2.6	7.6	...	20.8−21.4	1,2
1E 1048.1−5937	6.45	$\sim$3.81	$\sim$55	0.34	$\sim$5.0	$\sim$ 2.7	...	19.4−21.3	3,4
1E 2259+586	6.98	0.0483	0.55	1	0.59	230	CTB 109	20.4−21.7	5,6
4U 0142+61	8.69	0.196	1.2	0.33	1.3	70	...	19.8−20.2	7
1RXS J170849−400910	11.00	1.86	5.4	6.8	4.6	9.4	...	17.3	8
1E 1841−045	11.77	4.16	9.9	2.3	7.1	4.5	Kes 73	...	...
AX J1845.0−0258[c]	6.97	...	...	0.74	...	...	Kes 75	...	...
CXOU 010043.1−721134[c]	8.02	...	...	1.5	...	...	...	...	...

[a] References for near-IR magnitudes: [1] Israel et al. (2004); [2] Rea et al. (2004); [3] Wang & Chakrabarty (2002); [4] Durant & van Kerkwijk (2005); [5] Hulleman et al. (2001); [6] Tam et al. (2004); [7] Hulleman et al. (2004); [8] Israel et al. (2003)

[b] $\dot{P}, \dot{E}, B_s$ and τ_c values for this recently identified AXP are not confirmed.

[c] Unconfirmed candidate AXP

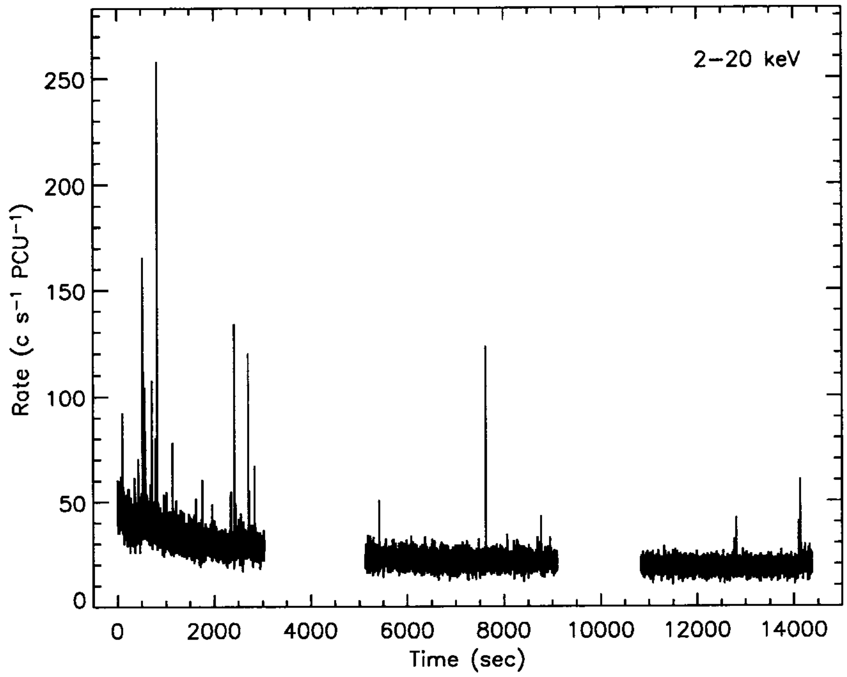

Figure 1.2: The 2–20 keV *RXTE* PCA light curve of 1E 2259+586 on 18 June 2002, binned at 1 s time resolution (Woods et al., 2004).

able (Gavriil et al., 2004). On 18 June 2002, >80 X-ray bursts were detected from 1E 2259+586 by Kaspi et al. (2003) with *RXTE* in a ~4 hour time period (see Figure 1.2). This major *outburst* saw a long-lived increase in the underlying pulsed X-ray luminosity above its value during quiescence that slowly decayed over a period of >1 yr, called the X-ray "afterglow", on top of which lay the many individual short bursts, the largest of which exceeded its pre-burst pulsed flux level (~0.25 counts/s/PCU in 2–10 keV, Woods et al., 2004) by >3 orders of magnitude. Several other X-ray properties were also affected; for instance, the pulsar glitched[1] nearly simultaneously with the onset of the outburst, and the pulse profile morphology and X-ray spectrum

[1]Glitches are sudden, unpredictable increases in pulse frequency, usually followed by gradual recovery to the previous value.

changed (Woods et al., 2004).

The next AXP to show SGR-like bursts was XTE J1810−197 (Woods et al. 2004, in preparation). This transient X-ray source was only recently discovered (Ibrahim et al., 2004) and identified as an AXP: the ~4 short burst events are indicative of AXP-like behaviour.

1.2.2 Optical/IR Properties

Near-infrared counterparts have been identified for five known AXPs: 1E 2259+586 (Hulleman et al., 2001), 1E 1048.1−5937 (Wang & Chakrabarty, 2002; Israel et al., 2002), 4U 0142+61 (Hulleman et al., 2004), 1RXS J170849−400910 (Israel et al., 2003), and XTE J1810−197 (Israel et al., 2004). The first counterpart discovered was that of 4U 0142+61; it is also the only AXP detected at optical wavelengths (Hulleman et al., 2000a), and exhibits pulsations in the optical band at the same period as the X-ray pulsar (Kern & Martin, 2002). All counterparts are fairly faint, with average K_s band (2.15 μm) magnitudes of ~20 (before correcting for interstellar absorption; see Table 1.1). They are identified as having large L_X/L_{IR} ratios, on the order of 1000 or higher, and stand out on colour-colour diagrams as redder than typical main sequence field stars. It should be mentioned that when the blackbody component of the X-ray spectrum is extrapolated to optical/IR frequencies, all five AXPs show an excess of emission; conversely, a power-law extrapolation from X-rays greatly overpredicts the expected flux. Possible IR emission mechanisms will be discussed in greater detail below.

1.3 Models of Emission for AXPs

As stated earlier, rotational spin-down has been eliminated as a possible X-ray emission mechanism on the basis that $L_X > \dot{E}$ in all cases. There is no evidence of AXPs having orbital companions, so binary accretion power is also ruled out. Below, I discuss the two main competing models for AXP emission.

1.3.1 Magnetar Model

The magnetar model was originally introduced in response to the unusual and unexplained behaviour of SGRs. In particular, it was the sudden and highly luminous soft gamma-ray bursts in conjunction with an uncommonly rotationally slow young pulsar located in a SNR that inspired the high magnetic field model (Mazets et al., 1979). Thompson & Duncan (1993) proposed that the mechanism powering these objects was the decay of high magnetic fields in excess of the "QED field" ($B_{QED} \equiv m_e^2 c^3/e\hbar = 4.4 \times 10^{13}$ G) belonging to energetic neutron stars, and outlined several arguments supporting high magnetization based on observed SGR properties (Thompson & Duncan, 1995); further evidence came with the first measurement of an SGR $\dot{P}$ which, through equation 1.3, revealed a magnetar-strength B_s field (Kouveliotou et al., 1998). Prompted by the many similarities between AXPs and SGRs, Thompson & Duncan (1996) speculated that burst activity might one day be detected in AXPs, a prediction that was satisfied not long afterwards. Recent magnetar reviews can be found in Duncan (2004) and Woods & Thompson (2004), and on the personal website of R. Duncan (http://solomon.as.utexas.edu/~duncan/magnetar.html).

Gamma-ray bursts and flares

It is thought that magnetars are born rapidly rotating, similar to ordinary pulsars, but with much larger initial spin frequencies. Differential rotation and convection in the star's fluid interior produce "dynamos" (magnetic field build-up through the rapid motion of charges) very early in magnetar evolution, which can rapidly create very strong dipole magnetic fields on the order of $10^{14} - 10^{15}$ G if the initial spin period is fast enough ($P_0 \sim 1$ ms, Thompson & Duncan, 1993; Duncan & Thompson, 1996).

Magnetic fields continue to move through the star's fluid interior. Drifting through the magnetar surface, an ultra-high magnetic field is capable of applying enough stress on the surface to cause crustal fractures if it exceeds a characteristic strength defined by the shear modulus μ of the crust: $B > B_\mu \equiv (4\pi\mu)^{1/2} \simeq 6 \times 10^{15}$ G near the base of the crust (Thompson & Duncan, 1995). The small but sudden displacement of the magnetic "footprints" (patches of crust where magnetic field lines are anchored) invokes an Alfvén[2] pulse that injects energy into the magnetosphere, and a simultaneous rapid rearrangement of magnetic field lines to a lower, less-tangled energy state: this is the source of the short, bright soft gamma-ray/hard X-ray bursts that all SGRs, and three AXPs, exhibit (Woods & Thompson, 2004, and references therein). A physical change in the structure of the crust is referred to as a "plastic", rather than elastic, deformation.

Giant flares, such as the events seen in SGR 0526−66 on 5 March 1979 (Mazets et al., 1979) and SGR 1900+14 on 27 August 1998 (Hurley et al., 1999; Thompson et al., 2000; Thompson & Duncan, 2001, and references therein), are thought to result from the same physical processes as the "normal" SGR bursts, but on much more extreme scales. Flares are characterised by enormous releases of energy, beginning with a <1 s spike of hard emission that peaks at a luminosity $>10^{44}$ erg/s, which is more than a million times the Eddington luminosity[3] of a neutron star. This spike is followed by a softer, persistent tail, referred to as the "soft tail", that lasts $\sim$100 s and

[2] Alfvén waves are the product of a displacement of magnetic field lines in a direction perpendicular to the lines. The restoring magnetic pressure gradient created by displacement acts to push the line back into place; this disturbance, similar to a wave on a string, propagates transversely along the field line (Carroll & Ostlie, 1996).

[3] The Eddington luminosity is the maximum radiative luminosity that a star can have and still remain in hydrostatic equilibrium.

shows periodic pulsations. A giant flare is possibly triggered when a highly distorted magnetic field in the star's core plastically deforms the interior crust from below, which twists the exterior field and induces magnetic reconnections (Thompson & Duncan, 1995, 2001); here, a comparatively larger amount of magnetic energy is released as the magnetar attempts to regain a new magnetospheric equilibrium, whereas the small bursts represent only minor crustal fractures.

The "trapped fireball" model attributes the soft gamma-ray, or hard X-ray, tail emission to an optically-thick plasma of $e^{\pm}$ pairs and thermal photons, originally ejected during the flare, anchored to the surface by a contracting surface bounded by the magnetosphere. The fireball fades with time as photons from the pair-producing/annihilating processes stream away from the gradually-shrinking outer layers. Observations show this emission is modulated at the rate of the rotating neutron star (Hurley et al., 1999).

Quiescent X-ray emission

Quiescent X-ray emission is powered by dissipation of the internal magnetic field: the amount of thermal X-ray flux at the surface can be estimated from the temperature at the core (Thompson & Duncan, 1996). Pulsed X-ray emission is predicted to originate from crustal hot spots located at the bipolar magnetic field footprints. Hot spots are produced by impacting electrons and protons that move with the strong induced currents along "globally twisted" magnetic field lines (global in the sense that entire hemispheres are twisted relative to each other, Thompson et al., 2002): as the heated patches cool, soft thermal X-rays are emitted. Hard, pulsed X-ray photons are thought to be generated when thermal surface X-rays are upscattered by rapidly moving current-carrying electrons (Thompson et al., 2002); however, the frequency and optical depth at which this "resonant cyclotron scattering" can occur is highly dependent on the local properties in the magnetosphere. Vacuum polarization affects thermal photons by suppressing the high-energy part of the blackbody spectrum, although a non-thermal tail is still observed due to non-grey opacities[4] (Ho & Lai, 2003, and references therein). Glitches in the timing of magnetars are also expected after a burst if an angular velocity gradient develops between the superfluid interior and recently fractured crust (Thompson & Duncan, 1996).

Optical/IR emission

The magnetar model does not yet make specific predictions for optical or near-IR radiation. However, Eichler et al. (2002) qualitatively address optical/IR emission in the context of the magnetar model to suggest that synchrotron emission from electrons and positrons in the outer magnetosphere could emit non-thermal pulsed radiation at optical or infrared wavelengths. This coherent, polarized emission represents a version of the beamed radio emission seen in ordinary pulsars, with scaled-up magnetospheric parameters. More recently, Özel (2004) shows synchrotron emission from a mono-distribution of electrons in the outer magnetosphere of a magnetar fits the optical spectrum of AXP 4U 0142+61.

1.3.2 Accretion Disk Model

Accretion from a debris disk surrounding the pulsar has been suggested as a model of the mechanism powering AXPs, the most popular of which incorporates a circumstellar fossil disk of material leftover by the progenitor supernova explosion. This fallback disk model could, under particular conditions, explain the narrow ranges of observed AXP characteristics. Chatterjee et al. (2000) break down the evolution of an accretion-disk pulsar into three

[4]Opacity is considered non-grey if its value is wavelength dependent.

phases: the "propeller", "tracking" and "ADAF" (advection-dominated accretion flow).

1. During the initial propeller phase, the pulsar rotation rate Ω is very large compared to the Keplerian rotation rate of the accretion disk, which is given by $\Omega_K(R_m) = \sqrt{GM/R_m^3}$, where R_m is the magnetospheric radius[5] and defines the innermost extent of the accretion disk. Although the mass accretion rate $\dot{M}$, defined as the rate by which mass is transfered from the disk towards the star, is large early on, it is also very inefficiently accreted due to the pulsar's large centrifugal forces, so most of the material never reaches the star before being ejected, and consequently the pulsar is X-ray dim (ie. mass accretion rate onto the surface $\dot{M}_X$ is small). These same forces are also the cause of the large decelerating torque that spins down the pulsar rapidly. This occurs on an estimated timescale of $t \sim 10^4$ yr.

2. The transition to the tracking phase occurs when Ω approaches $\Omega_K(R_m)$; here, the pulsar and disk are in quasi-equilibrium, material from the disk is successfully accreted, and the system becomes X-ray luminous ($\dot{M}_X \sim \dot{M}$) according to equation 1.5. Complete equilibrium is never attained because $\dot{M}$, and as a result L_X, are constantly decreasing. This is considered the relatively short ($\sim 10^4$ yr), bright AXP phase wherein observations are possible.

3. Accretion infall has been suggested to become "advection dominated", which causes mass ejection to occur once again, when the mass accretion rate and luminosity are of the order $0.01\dot{M}_E$ and $0.01L_E$, where $\dot{M}_E$ and L_E are the Eddington rate and luminosity, respectively (Chat-

[5] $R_m \approx 0.5r_A$ (Chatterjee et al., 2000), where the Alfvén radius r_A indicates the distance at which the magnetic energy density $U_M = B^2/8\pi$ becomes comparable to the kinetic energy density of the accreting matter $U_K = \frac{1}{2}\rho v^2$ (Carroll & Ostlie, 1996).

terjee et al., 2000, and references therein). During the ADAF phase, $\dot{M}_X < \dot{M}$ is continuously decreasing, and L_X decreases faster than $\dot{M}$. Eventually, the system becomes X-ray dim again.

Choosing arbitrary but plausible values for initial pulsar spin period $P_0 = 0.015$ s and total disk mass $M_d = 0.006\ M_\odot$, and assuming that for $\dot{M} \propto t^{-\alpha}$, $\alpha = 7/6$, Chatterjee et al. (2000) predict that fossil-disk pulsars with $B \sim 5 - 10 \times 10^{12}$ G will exist as AXPs with periods and X-ray luminosities in the range of those observed, on timescales that somewhat resemble observed characteristic ages ($\sim 10^4$ yr) . Furthermore, the changing $\dot{M}$ affects Ω in such a way as to mimic the spin-down of an ordinary rotation-powered pulsar.

Optical, infrared and submillimeter emission

Perna et al. (2000) model the time evolution of long-wavelength (optical to submillimeter bands) emission spectra from fallback-disk pulsars. Both viscous dissipation and reradiation of impinging X-rays from the central source contribute to the total energy output from the disk; however, for $L_X \gtrsim 10^{34}$ erg/s, which is the case in all observed AXPs, reradiation is the dominant source. If one assumes that the disk has a high opacity, which allows simplification of the emission to that of an optically thick blackbody, and that the effective temperature of the irradiated disk can be described by an analytic solution (Vrtilek et al., 1990), then under many of the same constraints set by Chatterjee et al. (2000), the predicted sub-mm flux of a few mJy is within the range of the SCUBA (Submillimeter Common-User Bolometer Array) instrument on JCMT (James Clerk Maxwell Telescope), and the predicted near-IR flux is generally above the J band limiting magnitude of $\sim$25 for NICMOS (Near-Infrared Camera and Multi-Object Spectrometer) on the *Hubble Space Telescope.*

1.4 1E 2259+586: An Overview

1E 2259+586 was the first AXP discovered (Fahlman & Gregory, 1981) and is located in SNR CTB 109. While at the time it was interpreted as a peculiar X-ray binary, its timing and spectral characteristics soon proved it to be otherwise. The properties of this source are quite typical for an AXP ($P = 6.98$ s, $L_X \sim 10^{35}$ erg/s), and it exhibits the most stable timing behaviour (Gavriil & Kaspi, 2002), which made the sudden discovery of its X-ray bursting episode in June 2002 all the more surprising (Kaspi et al., 2003). The outburst, which showed more activity than a single burst but was not as powerful as a giant flare, demonstrated that AXPs did indeed have a great deal in common with SGRs, as predicted uniquely by the magnetar model. The near-IR counterpart to 1E 2259+586 was suggested by Hulleman et al. (2001) with the Keck Observatory: a $K_s = 21.7 \pm 0.2$ magnitude source was seen in June 1999 coincident with the *Chandra* X-ray point-source position (see Figure 1.3 for its IR to X-ray spectrum). Shortly after the 2002 outburst, the near-IR flux more than tripled in concert with the X-ray enhancement: as the first example of correlated flux variability seen in an AXP (Kaspi et al., 2003), it opened new possibilities for studying the origins of IR emission.

In this thesis, I describe our continued monitoring program of the near-IR counterpart to 1E 2259+586 with the Gemini telescope, and report on the shared characteristics in flux variability detected at K_s band and X-ray wavelengths. I also discuss the impact of correlated activity on current AXP emission models, in particular, constraints that may be placed on the physical origins of both low and high frequency post-burst flux.

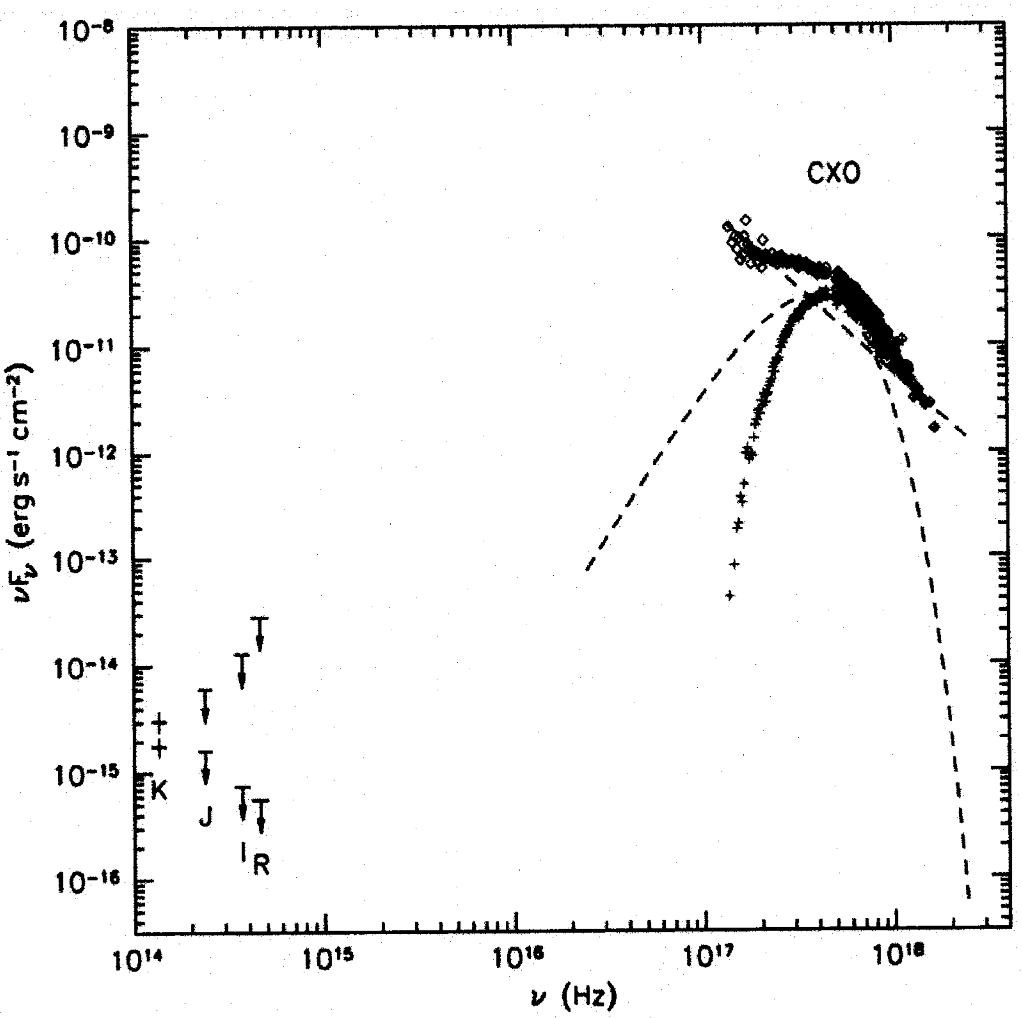

Figure 1.3: Broadband emission spectrum of 1E 2259+586, originally published in Hulleman et al. (2001). Denoted by CXO are the *Chandra* X-ray data (Patel et al., 2001): plus signs are absorbed and diamonds unabsorbed X-ray fluxes. Dashed lines show the blackbody and power-law components to the best-fit model. Also shown are the optical and infrared limits and the K_s band detection, as observed and after correction for interstellar reddening.

Chapter 2

The Gemini Observatory

2.1 Telescope and Site Information

The Gemini Observatory is an international collaboration between 7 partner nations that share time on each of its twin 8.1-meter telescopes. Canada is allocated approximately 14% of this optical/IR observatory's available time. The Gemini North Observatory is located on the summit of Mauna Kea in Hawaii at an altitude of more than 4 km, and Gemini South on Cerro Pachón in Chile at 2.5 km. At such high altitudes, and therefore low temperatures year round, Gemini is able to avoid many of the distorting atmospheric effects that degrade the quality of ground-based optical/IR astronomy. Each telescope is housed in a 45-meter high silver dome with an innovative ventilation system to provide a very stable thermal environment. Together, the two observatories provide nearly complete sky coverage, but as this project only required use of Gemini North, I will focus on its specifications.

The primary mirror, which is among the largest single-dish mirrors in the world, is 8.1 meters in diameter, 20 cm thick, and concave hyperboloid. The telescope is configured in a Cassegrain focus, which places the 1-meter secondary mirror in the reflected light's path before the focal plane, and

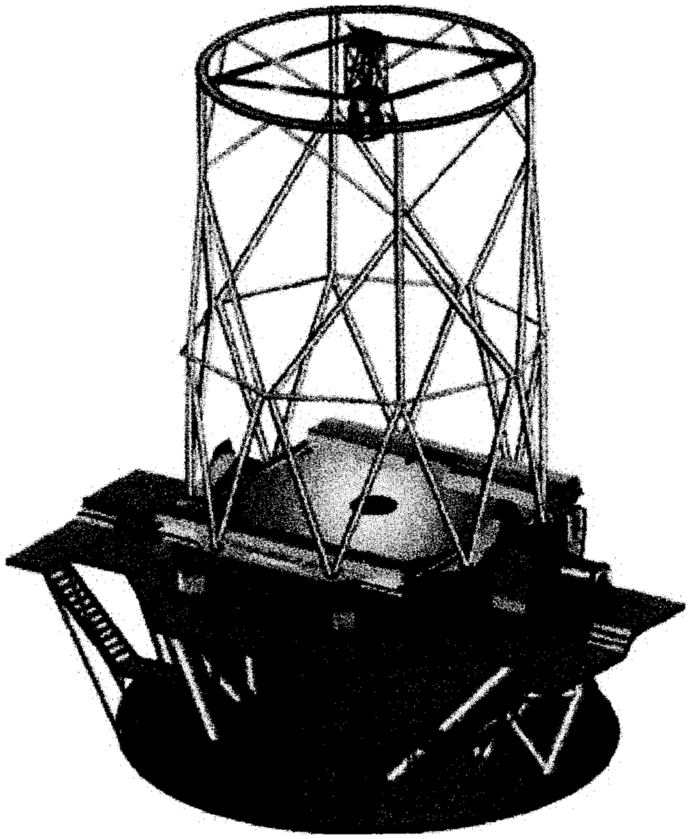

Figure 2.1: A schematic diagram of the Gemini telescope (from the Gemini Observatory/AURA website http://www.gemini.edu).

reflects it back through a hole in the primary mirror to the detector (see Figure 2.1). The convex hyperboloid surface of the secondary mirror also functions to extend the focal length. All mirrors have been coated in protected silver, which lowers the thermal emissivity of the telescope system, and consequently increases its sensitivity at IR wavelengths.

2.2 Instrumentation

Imaging and spectroscopic facilities are available in the optical ($\lambda \sim 0.3 - 1\ \mu$m), near-IR ($\lambda \sim 1 - 5\ \mu$m) and mid-IR ($\lambda \sim 8 - 25\ \mu$m) wavelength regimes. At Gemini North, there are three main science instruments currently in use: GMOS, Michelle, and NIRI.

The Gemini Multi-Object Spectrograph (GMOS) is an imager and spectrograph in the $0.36 - 1.1\ \mu$m optical range, which utilizes a multi-slit technique that enables spectroscopy of hundreds of objects in its $5.5'$ field-of-view. It is also equipped with an instrument known as an Integral Field Unit (IFU), which allows observers to perform integrated spectroscopy on extended objects 35 square arcseconds in size, at a spatial sampling of $0.2''$.

Michelle is Gemini's mid-IR imager and spectrograph, covering wavelengths $7 - 26\ \mu$m, and is shared with the United Kingdom InfraRed Telescope (UKIRT), also located on Mauna Kea. As an imager, its image quality approaches diffraction-limited resolution in this wavelength regime; that is, the full-width at half-maximum (FWHM) of the point spread function (PSF) is nearly $1.22\lambda/D$, where D is the diameter of the circular primary mirror. In spectroscopy mode, it is capable of a range of spectral resolutions, from low resolving power $R = \lambda/\Delta\lambda \sim 200$ to very high $R \sim 30000$.

2.2.1 NIRI

NIRI, the Near-Infrared Imager and spectrograph, was the instrument utilized in this analysis. Built by the University of Hawaii's Institute for Astronomy, it was originally commissioned for scientific use in 2001 but did not take any data until 2002. Later that year, NIRI suffered mechanical failures, but was recommissioned again before the beginning of 2003, and has functioned well since then. The instruments in NIRI are cryogenically cooled and mounted on the Gemini telescope's instrument support structure. For an indepth description of NIRI, see Hodapp et al. (2003). Key components of NIRI are summarized below, and shown in Figure 2.2.

- **Camera.** There are 3 cameras available on NIRI, named after their final focal ratios: f/6, for wide-field imaging and long-slit spectroscopy, f/14, for high-background imaging, and f/32, also for high-background imaging and adaptive optics imaging and spectroscopy. They have the following pixel scales and fields of view: $0.117''$ pixel^{-1}, $120'' \times 120''$ (f/6); $0.050''$ pixel^{-1}, $51'' \times 51''$ (f/14); $0.022''$ pixel^{-1}, $22'' \times 22''$ (f/32).

- **Detector.** The ALADDIN InSb detector array is 1024×1024 pixels in dimension, with each pixel 27-μm in size. It is sensitive to photons from 1 to 5.5 μm, and has a fairly uniform flat field response and low dark current. Figure 2.3 shows the detector uniformity as well as its imperfections; dead pixels, which account for approximately 0.1% of its pixels, are the result of photon-emitting defects and cracks in the array. The read noise level ranges from 13 to 200 e^-/pixel, depending on the background read mode. The gain is 12.3 e^-/ADU (Analog Digital Unit), and the quantum efficiency is $\sim$90%. The array is kept at the optical operating temperature of 33 K, which balances the contributions from read noise and dark current. Images are constructed by reading the array before and after the exposure, and taking the difference in charge between the reads.

- **Filters.** NIRI's broad-band filter wheel is located between the fold mirrors and the collimator in the optical path, and the narrow-band filter wheel is between the collimator and beam steerer #1 (see Figure 2.2). The filter wheel is 530 mm in diameter, and the filters themselves are 50 mm in diameter. The broad-band imaging filter set ($JHKK_sK'L'M'$) were acquired through the Mauna Kea Filter Consortium, a group consisting of roughly 30 member universities and observatories, which is attempting to optimize and standardize the characteristics of filters in near-IR astronomy. Typical bandpass properties include >80% average transmission with less than ±5% ripple on the peak transmission level, and out-of-band transmission of <0.0001 out to 5.6 μm (see Figure 2.4).

- **Spectrograph.** NIRI is also equipped with a moderate resolution spectrograph in the full $1 - 5.5$ μm range, but as this was an imaging analysis, I will not describe it further.

- **Adaptive Optics.** Gemini's recently commissioned adaptive optics system, Altair, is designed to be used with NIRI in f/32 mode, and is described in greater detail below.

2.2.2 Wavefront sensing

All observations with the Gemini telescope make use of the system's wavefront sensors (WFSs) which provide corrections for motion in the image and astigmatism, caused by such things as wind or stress, and require a guide star in the field of view of the sensor. The correction is applied through a tip-tilt motion on the secondary mirror, and surface manipulation of the thin primary mirror. This is known as "active optics". For further image improvement, Gemini North is now also equipped with an "adaptive optics" (AO) system, known as Altair, which corrects for the effects of atmospheric turbulence that degrade the effective seeing of the telescope. A model of the light wavefront is constructed from simultaneous observation of a nearby guide star, assuming that the statistical properties of the atmospheric distortion can be theoretically predicted. Information is fed back through the optical path, and a real-time correction is applied to the wavefront coming from the target object via manipulation of a 177-actuator deformable mirror

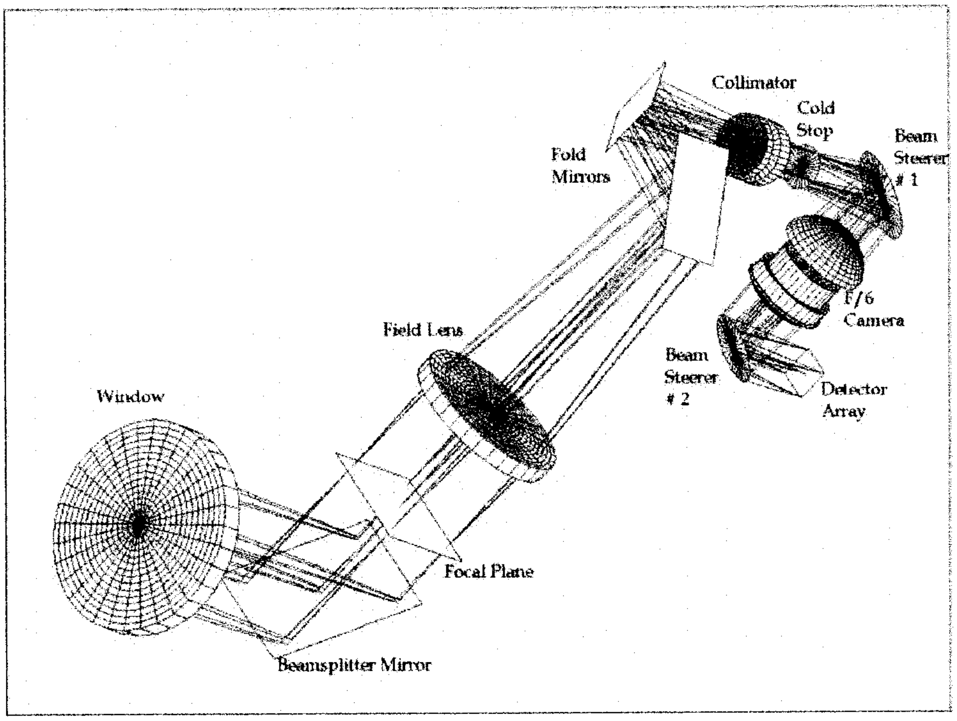

Figure 2.2: Optical path of the NIRI science module with f/6 camera system (Hodapp et al., 2003). The entrance window provides a 145 mm diameter clear aperture to the NIRI module. Not explicitly shown are the broad and narrow-band filter wheels, which are located between the fold mirrors and collimator, and collimator and beam steerer #1, respectively. The f/6 camera and ALADDIN detector array are described in §2.2.1.

and separate tip-tilt mirror. This "fast-guiding" occurs at a ~1 kHz correction rate. The goal is to improve the resolution to a nearly diffraction-limited level; specifically, if the median site seeing is typically 0.43″ at visible band wavelength $\lambda = 0.55$ μm, it is possible to achieve a resolution of $< 0.018''$ with adaptive optics.

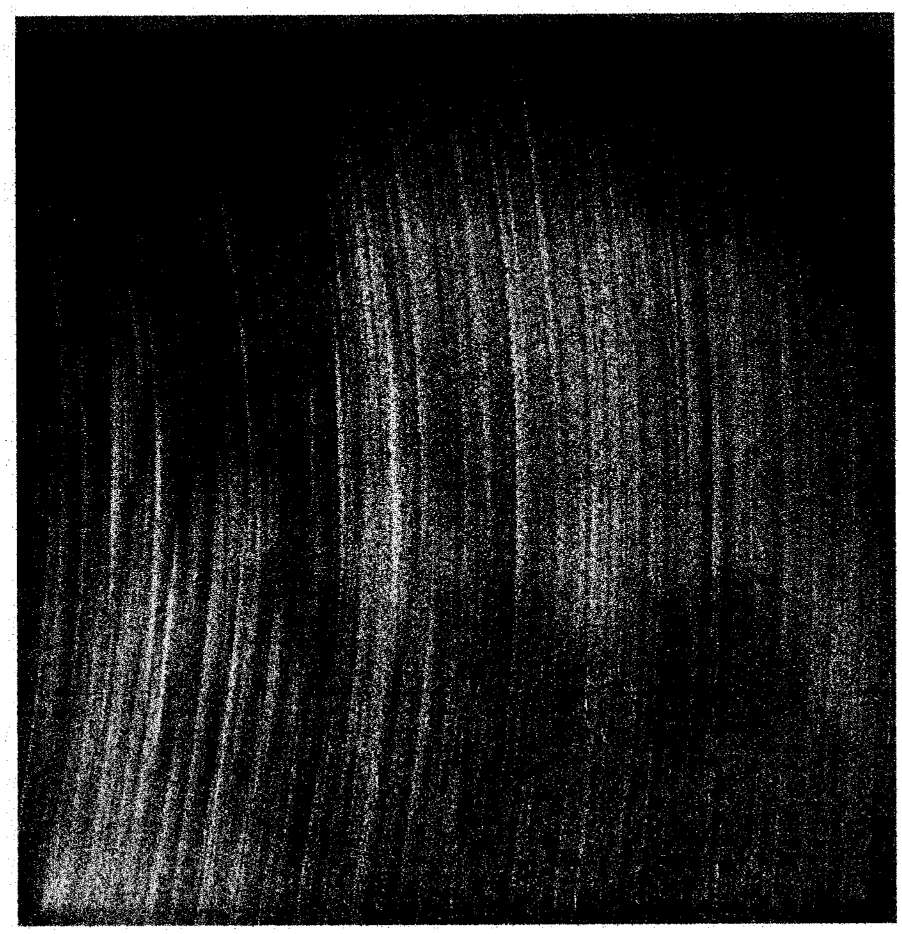

Figure 2.3: Example of ALADDIN detector array response uniformity. This K_s band flat field was taken 5 November 2003.

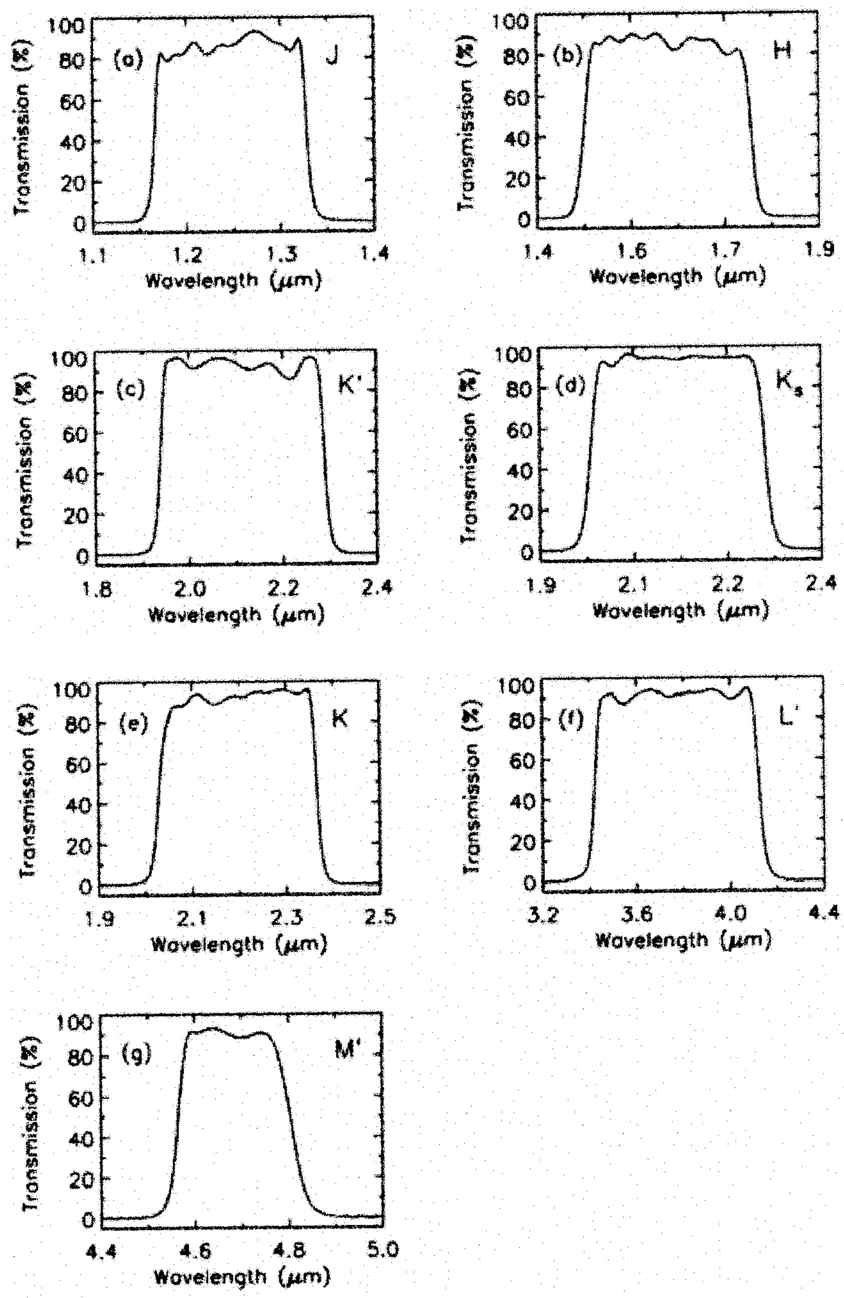

Figure 2.4: Gemini broad-band near-IR filter transmission profiles, as they would appear at a temperature of 65 K (Tokunaga et al., 2002).

Chapter 3

IRAF Software

The initial steps of optical and near-IR data analysis generally follow a standardized procedure. Here, I outline this process, focusing on how techniques are implemented through the multi-purpose software package IRAF, which stands for Image Reduction and Analysis Facility, developed by the IRAF programming group at the National Optical Astronomy Observatories (NOAO). A vast selection of manuals and tutorials on common procedures, as well as a detailed description of all tasks and packages, can be found on the IRAF project website (http://iraf.noao.edu).

3.1 Data Reduction

Before any measurements on optical and near-IR observations can be made, the raw data must be prepared through a process known as "data reduction". This calibration process exists to remove the mostly instrumental effects that all detector arrays of this sort are subject to; here, I will briefly describe the procedure (see Massey, 1997, for a complete tutorial). During the observation, it is likely that "bias", "flat" and possibly "dark" frames were also observed, in addition to the object frames which contain the target source itself: these are described below.

3.1.1 Bias and Dark Current

An additive effect that can set the overall signal level on a pedestal of several hundred ADU's too high, called the "floating bias", is the result of extra signal contributed by the electronics. The floating bias is usually measured from the "overscan region": generally a series of columns located at one side of the detector array. After the average signal in the overscan is subtracted from the array, the region itself is trimmed from the frame. This correction is applied to all data frames.

Bias, or "zero", frames are 0-s exposures that contain extra signal inherent to the electronic system, and can potentially vary from pixel to pixel. Usually, several bias frames are observed each night, and the average of these is subtracted from the object, flat and dark frames.

Another additive correction, that is often negligible and thus ignored, comes in the form of a dark current, or thermal noise from the system. This is a cumulative effect which does not scale linearly; therefore, the exposure length of the dark frame, which is observed with the telescope shutter closed, must be equal to that of the object frames.

3.1.2 Flat Fields and Bad Pixels

A normalized flat field frame is necessary to remove gain variations in the response of pixels across the detector, which are multiplicative in nature. With the shutter open, the detector array is exposed to some uniform source of illumination, either from a manufactured source of light, such as an illuminated white spot on the inside of the telescope dome, producing what is known as a "dome" or "lamp" flat, or from the twilight sky itself. Usually several flat fields are taken each night, and each is normalized to 1 ADU/s before they are combined into one averaged frame. All object frames must be corrected by dividing by the flat field. If multiple filters are being used, then a flat field in each filter is needed.

Finally, the object frames must be corrected for "bad pixels". These include both inherent defects in the detector (recall Figure 2.3), and cosmic-ray hits which are not instrumental at all but rather result from cosmological/extragalactic sources of high energy particles that cross the telescope's path at random. Generally, these can be "fixed" by interpolating over the affected regions. Defective pixels can be identified in a bad pixel "mask", while cosmic-ray hits are characterized by extremely strong spikes of signal localized to a very small area, typically one pixel.

Often, after data reduction, all object frames from a single night of observations are combined into one averaged frame; this improves the signal-to-noise level.

3.2 Photometry

IRAF contains several useful tools for performing photometry–that is, measuring an object's brightness. In general, there are two common techniques, known as aperture and point-spread-function (PSF) photometry. The former, which simply measures the amount of light intensity within a circular aperture of a certain size, may be appropriate for fields that do not contain many objects; however, in a crowded star field, any aperture large enough to contain most of the light belonging to an object will likely be contaminated by light from neighbouring sources, rendering this technique unsuitable. For this reason, a PSF photometry software package called DAOPHOT was developed by Stetson (1987), named so because it was introduced at the Dominion Astrophysical Observatory (DAO). The basic principle behind PSF photometry is that the two-dimensional intensity profile of stellar-like objects can be fit to a model (such as a Gaussian, for example), which can then be scaled and shifted to match the intensity and spatial position of all stars in the field. Each star's brightness is determined from the number of counts contained by the model PSF. DAOPHOT II, a updated algorithm, was eventually implemented in IRAF as a subpackage within the `noao.digiphot` package, with some minor variations from the original software (Massey & Davis, 1992; Davis, 1994).

3.2.1 Initializing the Software

Before running `daophot`, the user must input several critical algorithm parameters, such as an estimate of average FWHM for the image (`fwhmpsf`), the radius within which most of the flux from a PSF should be contained (`psfrad`), inner radius (`annulus`) and width of the annulus (`dannulus`) in which to measure sky background, standard deviation of the background (`sigma`), minimum and maximum acceptable pixel count values (`datamin`, `datamax`), and keywords indicating where in the image header `daophot` should look for instrument readout noise, gain, exposure time, airmass, filter, and observation time values.

A star list is created by the task `daofind`. This is a complex algorithm which searches for positive enhancements in the data that resemble stellar profiles, while excluding random noise peaks, such as defective pixels and cosmic-ray hits, and extended objects, such as galaxies. The detection threshold parameter `threshold` can be changed if the routine is finding an inappropriate number of stars (ie. only the brightest is too few, identifying noise spikes as stars is too many). It outputs the center x and y coordinates of every star candidate found, and assigns each an id number.

Next, the aperture photometry task `phot` is run non-interactively, which computes initial estimates of centers, sky values, and magnitudes for every object in the input sky list, and writes this and other information to the photometry file. If a star list is input, `phot` does not recompute new center coordinates and assumes they are known to be precise. Sky values are determined from data found within an annulus, defined by `annulus` and `dannulus`, around each star. The radius of the aperture (`apertures`) is typically set to be equivalent to `fwhmpsf`.

3.2.2 Determining the PSF

The model fitting routines require several isolated, bright (but not saturated) stars to act as template PSF's. The list is assembled by `pstselect` which can be run interactively or non-interactively. Ideally, these template PSF stars are distributed across the entire image, with the target-source region particularly well sampled.

The image, PSF star list, and initial photometry file are input to the PSF modelling task `psf`. It computes the best-fit analytic function based on all PSF stars, and records the residuals between the actual stellar profiles and the analytic function in a look-up table of corrections. At this point the user is given the option of choosing the type of function for the analytical component of the model: Gaussian, Moffat[1] or Lorentzian profiles are example options. Additionally, the user must specify whether the model is to be purely analytic, constant, linearly or quadratically variable with position in the image: the parameter `varorder` will dictate the number of look-up tables created. The initial run of `psf` is best done interactively so that the user is alerted of previously unnoticed unsuitable PSF star candidates, such as stars that have hidden neighbours, are saturated, or are diffuse or highly oblique in shape.

[1]A Moffat is a 2-D elliptical function that is a modified Lorentzian.

3.2.3 Profile Fitting

There are two common stellar subtraction algorithms. The first technique groups together stars in the region around each PSF star, and fits them simultaneously to the model as a group, using `nstar` and later `group`. The other technique groups, fits and subtracts all of the stars from the input image dynamically using `allstar`, which requires greater CPU time than the first method. With only four images to process, our computational power was such that time was not an issue; therefore, we chose the second method. `Allstar` outputs a new photometry file containing the recentered x, y positions, best fit magnitude and error, and the goodness-of-fit parameter `chi` for every star, as well as a residual image with all fitted stars subtracted. The task `substar` is then used to subtract all stars except for the PSF stars from the input image.

3.2.4 Improving the PSF Model

Usually, the first residual image produced is quite blotchy, indicating that most stars have not been well subtracted and the model is not good. Also, previously invisible stars near to the PSF stars may now become apparent. Upon examining either of the subtracted images, the next step would be to remove bad stars from the PSF star list with `pselect`, such as double stars, stars with underlying neighbours that can not be well subtracted, stars that lie on a cosmetic blemish, or stars with poor goodness-of-fit statistics (ie. large `chi`). Note that a PSF star with a sufficiently distant neighbour that looks like it could be better subtracted with an improved PSF model need not be removed from the list. New, faint stars revealed by subtraction of the brighter stars around can be marked and merged with the general photometry list using `phot`, `prenumber` and `pfmerge`.

Running `substar` again with the merged photometry list as input will produce a better subtracted image with only the isolated PSF stars remaining: this is input to the profile modelling algorithm `psf` again, which now constructs a (hopefully) much improved PSF. The new model is then fit to every star by `allstar` and subtracted from the input image. If the model still does not produce a smooth subtracted image, then the process beginning with `substar` in §3.2.3 is repeated as many times as necessary to produce a well modelled PSF, each time eliminating bad stars from the PSF list and adding previously invisible stars as needed. At the end of this iterative procedure, the photometry file produced by the best PSF model input to `allstar` will contain the final, uncalibrated magnitudes.

3.3 Calibration

Typically, one or more standard IR stars with well-established magnitudes are observed as close in time as possible to the target observations, for photometric calibration purposes. Good standard stars are bright and located in uncrowded fields so that aperture photometry can be used. Calibration involves correcting for several differences between the target and standard star. First, the "aperture correction" must be determined, which is the difference in magnitude between something measured through a large aperture, as used for the standard star, and a PSF of width `fwhm`, used for the target source. Other corrections include the "zero point", which is a constant term defined as the magnitude of a hypothetical point source emitting 1 ADU/s at an airmass[2] of 1. The zero point is an instrument and waveband dependent number needed to extract true magnitudes from instrumental magnitudes calculated by the software. Extinction, which is a measure of absorption by the Earth's atmosphere and is proportional to airmass, must be corrected

[2] Airmass is typically approximated as $\sec z$, where z is the angle between an object and the zenith.

for if the target and standard star were not observed at the same airmass. Finally, differences between the official "colours" (ie. spectral responsivity of optical/IR filters) of the standard system under which calibration stars are known and colours according to the particular instrument used in the observation can yield small measured offsets from the true magnitude.

Steps from this general procedure are sometimes omitted if the effect is negligibly small, or if an entirely different calibration technique is being used.

Chapter 4

Data Analysis

4.1 Observations

Observations of AXP 1E 2259+586 were obtained at four different epochs with the Gemini North telescope: observing parameters are summarized in Table 4.1. The first two, in June 2002, were Target of Opportunity (ToO) observations (Kaspi et al., 2003); that is, the Gemini Time Allocation Committee was appealed to for immediate response to X-ray detection of burst activity in 1E 2259+586, and awarded two observations with Gemini 3 and 10 days after the burst. Subsequent observations were spread over a $\sim$1.5 year period. Near-IR K_s-band ($\lambda = 2.15$ μm, $\Delta\lambda = 0.31$ μm; Figure 2.4) images were obtained with NIRI in f/6 camera mode. Unfortunately, Altair was not useful for this target due to the lack of nearby bright guide stars. Each target frame consisted of 4 coadded exposures of 15-s integrations, for an effective exposure length of 60 s. Short exposure lengths reduce saturation of the frame by the brightest stars in the field. The detector array was read several times and averaged to reduce read-out noise. This was done both before and after each exposure, and the difference was recorded in the data files: the bias is automatically removed through this technique. The frames

Table 4.1: Near-IR observing parameters.

Observation		Instrument	Exposure	Seeing	Band
Date	MJD		(min)		
2002 Jun. 21	52446.63	Gemini/NIRI	19	$0.7''$	K_s
2002 Jun. 28	52453.62	Gemini/NIRI	12	$0.5''$	K_s
2002 Aug. 18	52504.44	CFHT/AOB/KIR	122	$0.2''$	K'
2003 Aug. 11	52862.61	Gemini/NIRI	58	$0.5''$	K_s
2003 Nov. 5	52948.25	Gemini/NIRI	49	$0.3''$	K_s

were observed in a 9-point dither pattern, so that our target did not fall on the same detector pixels every time; this also permitted use of the actual target frames to construct the sky background. Flat fields with the shutter open and closed and 1-s dark frame observations were carried out by the Gemini Facility Calibration Unit on each night; these were used to create the normalized flat field and bad pixel map. Gemini data are by default stored in the form of multi-extension FITS (MEF) files, which consist of a Primary Header Unit (PHU) containing all important header information, and between 1 and 3 extensions containing pixel data.

The August 2002 observation, taken at the Canada France Hawaii Telescope (CFHT), was made by Israel et al. (2004) and published in a conference proceeding. This observation was made in K' band ($\lambda = 2.12\ \mu$m); however, because this is very close to K_s (see Figure 2.4) we have assumed $K' = K_s$ to simplify our analysis.

4.2 Performing the Data Reduction

Data reduction software specific to observational data from the Gemini telescopes has been conveniently integrated into IRAF as an external package.

We use the packages `gemini.niri` and `gemini.gemtools` which contain reduction tasks for NIRI data and generic tools for Gemini observations, respectively. These tasks are generally scripts that call other more standard IRAF tools, and allow flexible processing that can usually be optimized to preserve data quality for individual cases. Figure 4.1 shows an example of the reduction steps.

The first step in processing all NIRI data, calibration frames included, is to prepare the data using `nprepare`, which adds header keywords and information about the observation to the PHU. Next, `niflat` combines the calibration flats and darks to make the normalized flat field and a bad pixel map. A user-determined estimate of the FWHM of the PSF and all object frames from each night are input to `nisky`; this task then looks for star-like objects and flags them for masking/subtraction from the image to construct the sky background image. The advantage of sky background subtraction is that it allows one to better correct for the sky characteristics unique to that telescope and site. The sky image contains not only instrumental information, but also contaminating effects common to all observations for a particular night, such as light pollution from ground-based sources or persistent cloud cover, that reduce the telescope's sensitivity to the faintest sources. Additionally, less time and resources are lost to making separate calibration observations, since the sky is constructed from the actual data itself. As this particular project is a sky-limited observation, we ignore the effects of dark current. Finally, the task `nireduce` performs the flat division and sky subtraction on each science frame, and `imcoadd` averages the reduced frames together and cosmic-ray cleans the final images, which are shown in Figure 4.2.

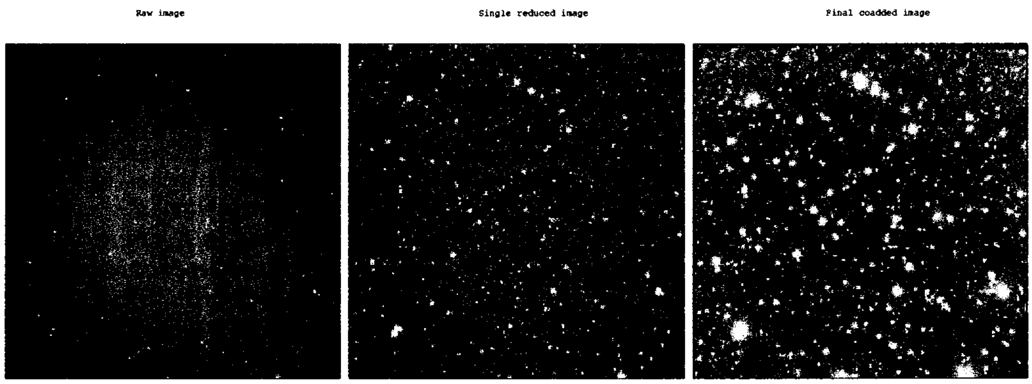

Figure 4.1: Example of step-by-step data reduction process. (*Left*) One raw K_s band 60-s exposure image from 5 November 2003. Note how the features and response of the detector are clearly visible. (*Centre*) The same image after reduction. Flat fielding and sky subtraction have produced a cleaner image with uniform background. (*Right*) Averaged image after combining 49 reduced frames from one night. Coadding has greatly improved the S/N, bringing out the faint sources.

4.3 Photometry Calibration

PSF photometry is performed according to standard procedures within the DAOPHOT package. Rather than calibrating the photometry on a single standard IR star, which typically returns errors on the order of 10%, we instead perform *relative* photometry, tying our measured instrumental magnitudes of field stars near 1E 2259+586 to the published values in Hulleman et al. (2001). Specifically, we choose the eight nearest neighbours that are bright, isolated and non-varying (stars A, B, B′, D, F, G, K and N under the numbering system of Hulleman et al., 2001), and measure the offset between instrumental and known magnitudes for all eight stars. We calculate the weighted mean offset and find the uncertainty on our value from the standard deviation of the weighted mean $\sigma/\sqrt{N}$, where $N = 8$ is the number of samples. To ensure non-variability, we use only those stars whose standard

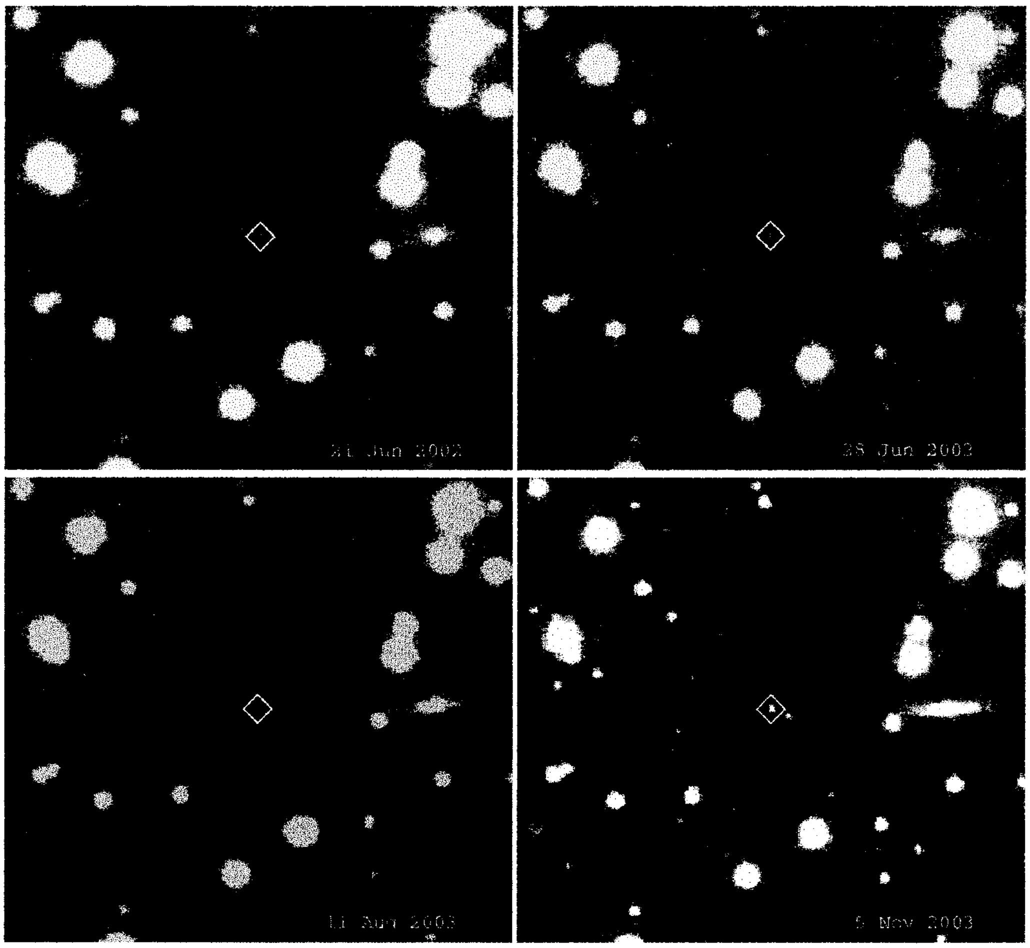

Figure 4.2: Gemini/NIRI final images in K_s band of the $\sim 25'' \times 25''$ region surrounding 1E 2259+586 (at the centre, indicated by diamonds), at four different post-burst epochs spanning 1.5 years.

deviation σ fall within 0.03 mag from the weighted mean offset.

4.4 Estimating the Uncertainties

The output from DAOPHOT includes estimated errors on measured magnitudes; however, we choose to analytically estimate errors based on the signal-to-noise (S/N) characteristics of our observations, and thus confirm the accuracy of those calculated by the software. We expect the S/N of sky background limited photometry to be

$$\frac{S}{N} \approx \frac{S \times 70\%}{\sqrt{A\sigma^2}} \tag{4.1}$$

where S is the total number of counts received from the star in ADU, A is the area contained within a circular aperture of diameter equal to the FWHM of the star's PSF in pixels, and σ is the RMS noise per sky pixel, as measured in a blank region near the star. Since each star's total counts are determined from its PSF profile, rather than a simple aperture, we estimate that only 70% of the flux will be accounted for in the area A. From the S/N, we calculate the uncertainties on the total star brightness in K_s magnitudes, and find our results agree well with DAOPHOT for the two observations in 2002 but less so in 2003, possibly because 1E 2259+586 is very faint by this time. These photometric errors are added in quadrature to the uncertainty from the relative calibration offset, to produce the final magnitudes listed in Table 4.2. We compare our magnitudes for the ToO data to those originally found by Kaspi et al. (2003) and find them consistent well within the uncertainties: the differences in K_s magnitude between the two analyses were 0.05 ± 0.17 (June 21) and 0.18 ± 0.25 (June 28).

4.5 Absorption Correction

Two effects, caused by dust in the interstellar medium, must be corrected for when determining an object's intrinsic brightness at optical and near-IR wavelengths: interstellar extinction, or absorption, and reddening. These effects are related, in that small-grained dust particles are more likely to scatter smaller-wavelength (bluer) light, thus reducing the total intensity of light received at Earth, and preferentially enhancing redder light.

To determine the absorption correction, we use the relationship between column density of hydrogen, N_H, and interstellar extinction in the visible band, A_V, given by Predehl & Schmitt (1995): $N_H/A_V = 1.79 \pm 0.03 \times 10^{21}$ atoms/cm^2/mag. Patel et al. (2001) find $N_H = 9.3 \pm 0.3 \times 10^{21}$ atoms/cm^2 for 1E 2259+586 by fitting its *Chandra* X-ray spectrum to a power-law plus blackbody model, giving $A_V = 5.2$ mag. From Cox (2000) we find

$$\frac{A_V}{E(J-K)} = 5.82 \pm 0.1 \quad \text{and} \tag{4.2}$$

$$\frac{A_\lambda}{E(J-K)} = 2.4(\lambda)^{-1.75} \quad (\text{for } 0.9 < \lambda < 6\ \mu\text{m}) \tag{4.3}$$

where $E(J-K) = (J-K)-(J-K)_0$ is known as the colour excess of $(J-K)$ due to reddening (the subscript "0" denotes dereddened, or unabsorbed, value). For $\lambda = 2.15$ (K_s band), $A_{K_s} = 0.56$ mag: this is the amount by which interstellar absorption has increased the magnitude of our measurements.

4.6 Converting to Flux

Apparent magnitude is a measure of relative brightness, defined by

$$\frac{\mathcal{F}_2}{\mathcal{F}_1} = 100^{(m_1-m_2)/5} \tag{4.4}$$

where $\mathcal{F}$ is the radiant flux of a star in erg/s/cm^2. Typically, Vega is used as the photometric standard for which we assume its magnitude $m = 0$ in all wavebands. From Cox (2000) its flux density is given as $F_\lambda(0) = 4.30 \times 10^{-7}$ erg/s/cm^2/μm in K_s band. To find F_λ of 1E 2259+586 at each epoch, we use equation 4.4: this is allowed despite the difference in units between $\mathcal{F}$ and F_λ because all our data are within the same waveband. Later in this analysis, it will be convenient to have a quantity in units that resemble flux, ie. erg/s/cm^2: this is achieved by converting F_λ to frequency-dependent units, F_ν (erg/s/cm^2/Hz), and multiplying by the frequency to obtain νF_ν. The final unabsorbed νF_ν values are listed in Table 4.2.

Table 4.2: K_s band photometry results showing time dependent flux decay data of 1E 2259+586.

Time (days post-burst)[a]	**Absorbed Magnitude** (mag)	**Unabsorbed νF_ν** (10^{-15} erg/s/cm^2)
3.50	20.41(7)	10.7 ± 0.7
10.49	20.96(14)	6.4 ± 0.8
61.31	21.31(24)	4.6 ± 1.0
419.38	21.66(11)	3.4 ± 0.3
505.12	21.54(5)	3.8 ± 0.2

[a]Glitch epoch $t_g = 52443.13$ MJD used as reference time.

Chapter 5

Results

The X-ray behaviour of 1E 2259+586 has been well described by Kaspi et al. (2003), Woods et al. (2004) and Gavriil et al. (2004). In analysing its near-IR post-outburst properties, we are particularly interested in the results of Woods et al. (2004) who characterize the *RXTE* long-term pulsed-flux time evolution in terms of a two-component power-law model. The $2 - 10$ keV pulsed flux F (where $F \propto t^{\alpha}$ is dependent on time post-glitch t) was observed to decay very rapidly immediately following the outburst ($t < 1$ day), with a steep power-law index α. After $t = 1$ day, the pulsed-flux continued to decay but at a much slower rate; this long-term (>1 yr) slow decay of the pulsed-flux enhancement is referred to as the X-ray "afterglow".

The goal of this analysis is to compare the long-term post-burst characteristics of 1E 2259+586 in the near-IR and X-ray, paying close attention to the question "can the observed IR variability be undeniably linked to the X-ray outburst of June 2002, or is it merely a coincidence?" We attempt to address this by fitting the near-IR data to two flux decay models, and comparing the best-fit parameters to those produced by similar fits to the corresponding X-ray data. This original work has also been published in Tam et al. (2004).

5.1 Power-law model

We first fit the data to a simple power-law function, similar to that used by Woods et al. (2004):

$$F = k\left(\frac{t}{100}\right)^{\alpha} \tag{5.1}$$

where t is time in days since the glitch epoch (t_g = 52443.13 MJD), α is the temporal decay index, k is a constant with dimensions erg/s/cm^2, and the factor of 100 roughly minimizes the covariance between k and α. It is important to note that F represents either X-ray flux (Table 5.1) or near-IR νF_ν (Table 4.2), depending on the case, in erg/s/cm^2. Also, we choose the glitch epoch as our reference time for fitting because, unlike the time of the beginning of the outburst, it is well determined to high accuracy through glitch modelling (Woods et al., 2004).

The fitting is performed by a numerical χ^2 fitting routine that directly searches over parameter space. The best-fit parameter values and corresponding 1σ uncertainties are shown in Table 5.2. Note that in some cases, the data uncertainties have been scaled (upwards) such that the reduced χ^2, denoted by $\tilde{\chi}^2$, is equal to 1; it is from this adjusted data that parameter uncertainties are inferred, although the listed χ^2 reflects their value before rescaling. Figure 5.1 shows the data with the best-fit power law curves (dashed lines) overplotted.

We find the power-law indices between the two data sets remarkably consistent: $\alpha = -0.21 \pm 0.01$ (X-ray) and -0.21 ± 0.02 (IR). Additionally, our results agree with the afterglow index reported by Woods et al. (2004) of $\alpha = -0.22 \pm 0.01$. The small discrepancy can be explained by noting that Woods et al. (2004) perform a χ^2 fit on log-log data to a linear function, which neglects to account for asymmetric uncertainties, unlike our numerical method. This confirms that the X-ray afterglow and near-IR flux decay at a similar rate.

Table 5.1: *RXTE* 2–10 keV pulsed-flux X-ray data, originally from Figure 13 of Woods et al. (2004).

Time MJD	**Flux** (10^{-11} erg/s/cm^2)
51613.81	1.56 ± 0.10
51676.21	1.55 ± 0.13
51718.31	1.62 ± 0.13
51760.59	1.71 ± 0.11
51802.67	1.40 ± 0.11
51844.61	1.77 ± 0.11
51886.14	1.63 ± 0.10
51932.62	1.70 ± 0.12
51970.08	1.81 ± 0.15
52016.01	1.84 ± 0.13
52058.94	1.54 ± 0.10
52099.87	1.65 ± 0.10
52142.07	1.62 ± 0.12
52184.43	1.70 ± 0.12
52233.53	1.45 ± 0.12
52270.19	1.66 ± 0.16
52312.22	1.53 ± 0.13
52355.35	1.41 ± 0.09
52398.39	1.39 ± 0.09
52445.06	5.09 ± 0.28
52449.32	4.10 ± 0.18
52455.12	3.97 ± 0.23
52455.59	4.10 ± 0.24
52457.02	3.76 ± 0.22
52461.84	3.37 ± 0.27
52461.91	3.42 ± 0.27
52461.97	3.25 ± 0.26
52503.04	2.68 ± 0.09
52509.87	2.71 ± 0.10
52518.70	2.50 ± 0.12
52528.59	2.38 ± 0.12
52535.50	2.26 ± 0.11
52543.47	2.51 ± 0.12
52548.36	2.28 ± 0.10
52553.92	2.23 ± 0.11
52560.75	2.21 ± 0.11
52568.53	2.21 ± 0.16
52575.51	1.98 ± 0.15
52595.52	2.10 ± 0.12
52638.17	1.80 ± 0.11
52653.97	2.19 ± 0.10
52667.36	1.97 ± 0.11
52686.04	1.78 ± 0.13
52713.67	1.80 ± 0.12
52728.22	1.96 ± 0.13
52743.98	1.76 ± 0.14
52758.53	1.95 ± 0.15
52772.97	2.31 ± 0.18

Table 5.2: Results of power-law and excess function fitting.

Model	F_q (erg/s/cm^2)	k (erg/s/cm^2)	f	α	χ^2	$\tilde{\chi}^2$
X-ray PL	...	$(2.35 \pm 0.02) \times 10^{-11}$	...	-0.21 ± 0.01	37.1^a	1.0
IR PL	...	$(5.02 \pm 0.25) \times 10^{-15}$	...	-0.21 ± 0.02	7.1^a	1.0
X-ray excess	$(1.56 \pm 0.03) \times 10^{-11}$	...	2.14 ± 0.14	$-0.44^{+0.34}_{-0.03}$	97.3^a	1.0
IR excess	$(3.49^{+0.22}_{-0.37}) \times 10^{-15}$	...	$2.05^{+0.34}_{-0.25}$	$-0.75^{+0.22}_{-0.33}$	1.4	0.5
	$(3.04 \pm 0.09) \times 10^{-15}$	...	2.14 (fixed)	-0.44 (fixed)	5.7	1.1

[a]Errors scaled to infer uncertainties on the parameters. χ^2 values reflect those before rescaling.

5.2 Excess function model

At $t = 1$, there is a noticeable similarity between the X-ray and near-IR flux enhancements above the quiescent flux level F_q. In order to quantify this, we perform a χ^2 fit on the data to a second function consisting of a power-law with an excess offset

$$F = F_q \left(1 + f \left(\frac{t}{t_0}\right)^{\alpha}\right) , \tag{5.2}$$

where $t_0 = 3.50$ days is the time since the glitch of the first IR observation, $f = (F_0 - F_q)/F_q$ is the flux excess, and F_0 is the flux enhancement at t_0. We include data from $t < 0$ for fitting the quantity F_q; these include X-ray points occurring prior to 52443 MJD in Table 5.1, and the single near-IR detection on 51353 MJD of $\nu F_\nu = 3.34 \pm 0.59 \times 10^{-15}$ erg/s/cm^2 (Hulleman et al., 2001).

From Table 5.2, we see that the best-fit f values are consistent between X-ray and IR data, indicating that shortly after the burst, the flux increased by the same factor at both wavelengths. However, large uncertainties and $\tilde{\chi}^2 < 1$, produced by fitting three parameters to a small number of near-IR data points, prompted a secondary check of the statistical consistency of our results. We re-fit the K_s data to the excess model with α and f fixed at the best-fit X-ray numbers. The effect of holding two parameters constant is an increase in $\tilde{\chi}^2$ to 1.1, showing that, within uncertainties, the shapes of the two decay curves are indeed consistent with each other. In Figure 5.1 we plot the power-law plus excess model for $\alpha = -0.44$ and $f = 2.14$ (dot-dashed lines) over the X-ray and K_s data, and the corresponding F_q best-fit value (dotted lines), for comparison.

Having found that the X-ray and near-IR fluxes increased by nearly the same factor immediately following the 2002 outburst, and subsequently decayed at very similar rates, we can state with confidence that the data are highly correlated.

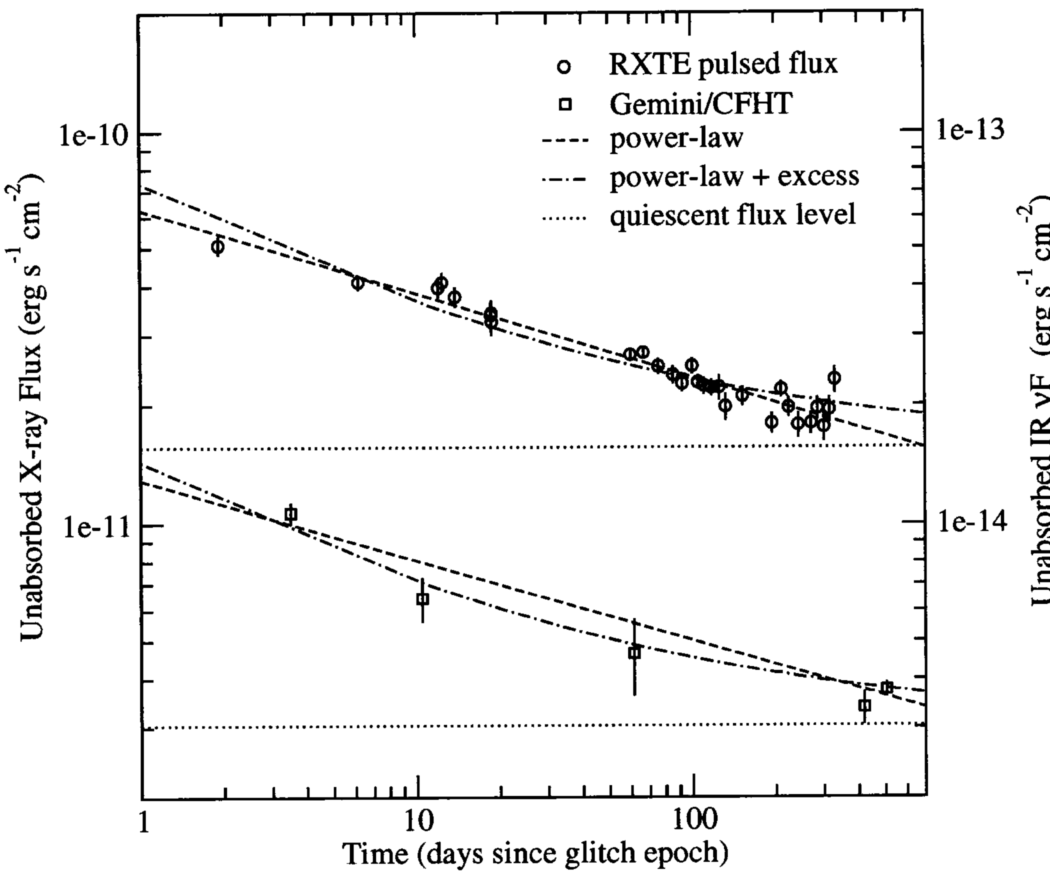

Figure 5.1: Unabsorbed X-ray flux and near-IR νF_ν decay of 1E 2259+586 as a function of time (Tam et al., 2004). *RXTE* pulsed flux data are represented by circles and refer to the left axis, Gemini and CFHT data are represented by squares and refer to the right axis. Best-fit power laws to the X-ray and near-IR data are shown in dashed lines. The power-law plus excess model, with α and f fixed at the best-fit X-ray values 2.14 and -0.44 respectively, is shown in dot-dashed lines; the dotted lines denote the flux level during quiescence as determined by the excess function fit.

Chapter 6

Discussion

In this chapter, I compare our results with other AXPs and discuss them in the context of various models. The work presented here was originally presented in Tam et al. (2004).

6.1 Accretion Disk vs. Magnetar Model

It has been suggested that fossil disk accretion could be the source of emission from AXPs (see §1.3.2; Chatterjee et al., 2000; Perna et al., 2000). However, this model fails to explain a number of important phenomena, such as the SGR-like bursts now observed in three AXPs (§1.2.1): rapid X-ray variability on burst timescales simply can not be attributed to steady accretion of material from disk to star. A recent report by Gavriil & Kaspi (2004) showed uncorrelated X-ray flux and torque variations in 1E 1048.1−5937. The detection of long-term X-ray flares which are only marginally correlated to *decreases* in the pulsar's spin-down contradicts the expectation of a strong positive correlation between L_X and $\dot{\nu}$ in accretion scenarios (Chatterjee et al., 2000). The ratios of X-ray to optical R band (Hulleman et al., 2000b) and K_s band (Hulleman et al., 2001) flux measured in 1E 2259+586 are exceptionally high; similarly, the near-IR J band counterpart to 1RXS J170849−400910 discovered by Israel et al. (2003) is much dimmer than expected for a disk model. Ertan & Cheng (2004) show that the high optical pulsed fraction seen in 4U 0142+61 (Kern & Martin, 2002) can be accounted for by either the magnetar outer gap model or the disk-star dynamo gap model; however, whether the latter is able to produce bursts is unclear.

Ekşı & Alpar (2003) argue that accretion disk models need not be abandoned entirely if one considers a "hybrid" scenario, wherein a highly magnetized neutron star is surrounded by a thin fallback disk. In the hybrid model, bursts and optical pulsations must originate in the magnetar-like crust or magnetosphere, but all other properties are produced in the disk. However, if enhanced X-ray radiation and modifications to the spin evolution originate from a disk that has had its inner regions pushed back to larger radii by a giant SGR flare, as suggested by Ertan & Alpar (2003), then the hybrid model still fails to explain the X-ray enhancement of 1E 2259+586, from which no giant flare was observed (Woods et al., 2004).

Although correlated activity between X-ray and IR radiation is a natural prediction of the accretion disk model (Rea et al., 2004, and references therein) due to the overall increase in disk temperature from an increase in L_X, the unexplained phenomena mentioned above strongly argue against it. Since the majority of the evidence available favours the magnetar model as the source of emission from AXPs, we will focus on it in our discussion.

6.2 Possible Sources of IR Emission

Thermal emission has been ruled out as the source of optical/IR emission because it would require a much higher surface brightness temperature than is currently implied by X-ray spectra (Özel, 2004). This implies that it must be magnetospheric in origin. In §1.3.1, we outline recent work by Eichler et al.

(2002) and Özel (2004) who suggest synchrotron emission from electrons and positrons in the magnetosphere may be responsible for the optical/IR spectrum. X-ray emission produced by resonant scattering is very dependent on the configuration and strength of field lines in the magnetosphere (Thompson et al., 2002). IR radiation from synchrotron processes would also depend heavily on local magnetospheric conditions; therefore, if the magnetosphere were to undergo some sort of physical restructuring, one might expect a correlation between changes in X-ray and IR emission. Unfortunately, there are currently no publications explicitly describing correlated activity in magnetars; however, we understand that future work by C. Thompson includes ideas on this matter.

Although the physical origins of optical/IR photons have been narrowed down, the *mechanism* producing them is still not certain. Specifically, it is still possible that long-wavelength photons could be rotation powered, despite the X-ray emission being far too luminous to be so: recall for 1E 2259+586, $L_X \sim 10^{35}$ erg/s in 1$-$10 keV, assuming a distance of ~4 kpc, whereas $\dot{E} = 5.5 \times 10^{31}$ erg/s (Table 1.1). Current optical data of 4U 0142+61 do not exclude a rotational energy source (see Figure 1 of Özel, 2004). However, upon examination, we find a rather large implied efficiency of conversion from spin-down (Özel, 2004, equation 2) to optical (unabsorbed $V = 20.25$ mag; Hulleman et al., 2000a) flux:

$$\frac{\nu F_{\nu,V}}{\nu F_{\nu,rot}} \approx \frac{1.5 \times 10^{-13}}{2.7 \times 10^{-13}} \approx 0.55 \tag{6.1}$$

which argues against, though does not disprove, this hypothesis. It has been suggested that observations of magnetars in the UV spectrum could help narrow down the nature of the emission processes.

6.3 Constraining the Magnetar Model

Regardless of uncertainties in IR emission mechanisms, we can still use the correlation to clarify the origins of X-ray afterglow emission. Woods et al. (2004) identified two possible mechanisms that may have produced sustained, pulsed X-ray emission following the 2002 outburst.

The first mechanism involves a genuine thermal afterglow, wherein photons injected from the magnetosphere during an outburst impulsively heat the crustal surface, which cools over an extended period of time. This argument has been invoked to describe the X-ray afterglows of SGRs that exhibit bright, soft gamma-ray flares (Kouveliotou et al., 2003); however, no similar giant impulse of energy in the form of a fireball-driven "spike" was detected by either *RXTE* or the Konus detector aboard the *Wind* spacecraft which maintained continuous coverage of 1E 2259+586 beginning before the glitch epoch (Woods et al., 2004).

Alternatively, long-term enhanced X-ray emission may result from the same mechanism as SGR bursts, that is, twisting magnetic field lines connected to restructuring of the neutron star surface at the footpoints (§1.3.1). The observed rotational glitch that occurred nearly simultaneously with the outburst supports the scenario of a sudden deformation of the crust (Kaspi et al., 2003; Woods et al., 2004), as do observed changes to the X-ray spectrum and pulse profile, thought to be a result of a change in the state of currents in the magnetosphere (Thompson et al., 2002). A natural result of such an event would be an increase in X-rays, with the slowly decaying afterglow attributed to gradual relaxation of the twisted B field. Our argument linking the physical origins of the correlated X-ray afterglow and IR emission to the magnetosphere agrees qualitatively with this model: if the IR flux is indeed from $e^{\pm}$ pairs in the magnetosphere, then an enhancement and subsequent decay is consistent with relaxation of a recently twisted field.

In the event of a future outburst, it would be revealing to look for polarization and pulsations in the IR flux, as a discovery of the former would support the synchrotron scenario and the latter would argue in favour of a local magnetospheric disturbance. A similar IR pulse morphology to that in X-rays would be highly significant, particularly if correlated changes are detected.

6.4 IR Variability in Other AXPs

1E 2259+586 is not the only AXP that has demonstrated variability at optical/IR wavelengths, although it was the first example to show such behaviour associated with X-ray bursting activity (Kaspi et al., 2003). Reported variability has been reported for three other AXPs.

1E 1048.1−5937 was observed twice in early 2002, during which its K_s band magnitude changed from >20.7 (Israel et al., 2002) to 19.4 (Wang & Chakrabarty, 2002), a brightening of >1.3 magnitudes in less than two months time. Contemporaneous *RXTE* monitoring showed that although this AXP is known to be highly X-ray active (Gavriil et al., 2002; Gavriil & Kaspi, 2004), no X-ray activity occurred between the two epochs. Recent detections throughout 2003 indicate that it has returned to a stable low IR emission level ($K_s \sim 21.3$, Durant & van Kerkwijk, 2005) which may represent its quiescent state between burst episodes; however, broad X-ray flares[1] during 2003 put its X-ray flux at this time slightly higher than it was at the epoch of its 2002 brightening, quite the opposite of what we would expect if flux changes between X-ray and IR are normally correlated. In a similar fashion, the K_s band emission of 4U 0142+61 varied between 19.7 and 20.2 magnitude during 1999−2002 (Hulleman et al., 2004), despite evidence of X-

[1]The term "flare" is used here loosely. The events reported by Gavriil & Kaspi (2004) are much longer lived and less energetic than the giant SGR flares.

ray stability during the same time (Gavriil & Kaspi, 2002, and unpublished work). It is true that small bursts may have occurred in between *RXTE* observations; however, the frequency of AXP monitoring observations is such that significant activity on the scale of an outburst would not be missed. This contrast to the correlated behaviour of 1E 2259+586 suggests that the physical mechanism responsible for IR emission in AXPs is independent of that which produces *quiescent* X-rays, including those produced during broad flaring events.

The conclusion that post-outburst X-ray and near-IR emission are generally correlated is further supported by recent results from Rea et al. (2004) who detect similarities in the flux variability of XTE J1810−197. The K_s band flux of this transient AXP decayed by ~0.5 magnitudes since its initial detection 5 months prior (Israel et al., 2004), following the same trend as its X-ray emission which brightened suddenly (Ibrahim et al., 2004; Gotthelf et al., 2004) and has been fading ever since (Halpern & Gotthelf, 2004). What distinguishes the transient nature of this AXP from the outburst event seen in 1E 2259+586 is still a mystery.

Chapter 7

Conclusions

With the Gemini telescope, we have observed the near-IR magnitude of 1E 2259+586 over a period of ~1.5 years following its X-ray outburst on 18 June 2002. Using photometry, we measured the post-burst K_s band flux, and find that after an initial increase by a factor of >3, it decayed in concert with pulsed X-ray "afterglow" emission seen by the *Rossi X-ray Timing Explorer.* When characterized as power-laws, the best-fit decay indices to the IR and X-ray data are nearly identical, indicating that both types of emission faded at the same rate. Furthermore, we find the enhancement of the IR flux above its quiescent, pre-burst level is statistically well described by the best-fit parameters that describe the X-ray afterglow, which implies that they brightened by the same factor following the outburst and will return to quiescence on similar timescales. This evidence is highly suggestive of a correlation between the post-outburst behaviour of the near-IR flux and X-ray afterglow.

The magnetar model describes the emission from soft gamma repeaters, and now anomalous X-ray pulsars as well, as the product of a neutron star with exceptionally high magnetization. Our result, in the context of the magnetar model, constrains the physical origins of enhanced radiation following bursting activity to the magnetosphere, rather than surface. Optical/IR decay correlated with X-ray emission has been detected in another AXP, although the opposite behaviour seen in two others suggests that the IR producing emission mechanism is somehow unique from the mechanism responsible for X-rays during quiescence. Finally, we find our observations consistent with early, qualitative AXP models attributing optical/IR emission to magnetospheric synchrotron radiation, and hope that they may contribute further to constraining and developing the magnetar model.

Bibliography

Carroll, B. W. & Ostlie, D. A. 1996, An introduction to modern astrophysics (Reading, Mass. : Addison-Wesley Pub., c1996.)

Chatterjee, P., Hernquist, L., & Narayan, R. 2000, ApJ, 534, 373

Cox, A. N., ed. 2000, Allen's astrophysical quantities, 4th ed. (New York: AIP Press; Springer)

Davis, L. E. 1994, A Reference Guide to the IRAF/DAOPHOT Package, NOAO, Tucson, Arizona

Duncan, R. C. 2004, in 3-D Signatures in Stellar Explosions, ed. P. Hoeflich, P. Kumar, & J. C. Wheeler (Cambridge University Press), in press (astro-ph/0401415)

Duncan, R. C. & Thompson, C. 1996, in AIP Conf. Proc. 366: High Velocity Neutron Stars, ed. R. E. Rothschild & R. E. Lingenfelter (New York: AIP Press), 111

Durant, M. & van Kerkwijk, M. H. 2005, ApJ, submitted

Eichler, D., Gedalin, M., & Lyubarsky, Y. 2002, ApJ, 578, L121

Ekşı, K. Y. & Alpar, M. A. 2003, ApJ, 599, 450

Ertan, Ü. & Alpar, M. A. 2003, ApJ, 593, L93

Ertan, Ü. & Cheng, K. S. 2004, ApJ, 605, 840

Fahlman, G. G. & Gregory, P. C. 1981, Nature, 293, 202

Gavriil, F. P. & Kaspi, V. M. 2002, ApJ, 567, 1067

Gavriil, F. P. & Kaspi, V. M. 2004, ApJ, 609, L67

Gavriil, F. P., Kaspi, V. M., & Woods, P. M. 2002, Nature, 419, 142

—. 2004, ApJ, 607, 959

Gotthelf, E. V., Halpern, J. P., Buxton, M., & Bailyn, C. 2004, ApJ, 605, 368

Halpern, J. P. & Gotthelf, E. V. 2004, ApJ, in press (astro-ph/0409604)

Ho, W. C. G. & Lai, D. 2003, MNRAS, 338, 233

Hodapp, K. W., Jensen, J. B., Irwin, E. M., Yamada, H., Chung, R., Fletcher, K., Robertson, L., Hora, J. L., Simons, D. A., Mays, W., Nolan, R., Bec, M., Merrill, M., & Fowler, A. M. 2003, PASP, 115, 1388

Hulleman, F., Tennant, A. F., van Kerkwijk, M. H., Kulkarni, S. R., Kouveliotou, C., & Patel, S. K. 2001, ApJ, 563, L49

Hulleman, F., van Kerkwijk, M. H., & Kulkarni, S. R. 2000a, Nature, 408, 689

Hulleman, F., van Kerkwijk, M. H., & Kulkarni, S. R. 2004, A&A, 416, 1037

Hulleman, F., van Kerkwijk, M. H., Verbunt, F. W. M., & Kulkarni, S. R. 2000b, A&A, 358, 605

Hurley, K., Cline, T., Mazets, E., Barthelmy, S., Butterworth, P., Marshall, F., Palmer, D., Aptekar, R., Golenetskii, S., Ill'lnskii, V., Frederiks, D., McTiernan, J., Gold, R., & Trombka, T. 1999, Nature, 397, 41

Ibrahim, A. I., Markwardt, C. B., Swank, J. H., Ransom, S., Roberts, M., Kaspi, V. M., Woods, P. M., Safi-Harb, S., Balman, S., Parke, W. C., Kouveliotou, C., Hurley, K., & Cline, T. 2004, ApJ, 609, L21

Israel, G. L., Covino, S., Perna, R., Mignani, R., Stella, L., Campana, S., Marconi, G., Bono, G., Mereghetti, S., Motch, C., Negueruela, I., Oosterbroek, T., & Angelini, L. 2003, ApJ, 589, L93

Israel, G. L., Covino, S., Stella, L., Campana, S., Marconi, G., Mereghetti, S., Mignani, R., Negueruela, I., Oosterbroek, T., Parmar, A. N., Burderi, L., & Angelini, L. 2002, ApJ, 580, L143

Israel, G. L., Rea, N., Mangano, V., Testa, V., Perna, R., Hummel, W., Mignani, R., Ageorges, N., Lo Curto, G., Marco, O., Angelini, L., Campana, S., Covino, S., Marconi, G., Mereghetti, S., & Stella, L. 2004, ApJ, 603, L97

Israel, G. L., Stella, L., Covino, S., Campana, S., Angelini, L., Mignani, R., Mereghetti, S., Marconi, G., & Perna, R. 2004, in Young Neutron Stars and Their Environments, IAU Symposium 218, ed. B. Gaensler & F. Camilo (San Francisco: Astronomical Society of the Pacific), in press (astro-ph/0310482)

Kaspi, V., Gavriil, F., Woods, P., & Chakrabarty, D. 2004, The Astronomer's Telegram, 298, 1

Kaspi, V. M. & Gavriil, F. P. 2004, in The Restless High-Energy Universe, ed. E. van den Heuvel, J. in't Zand, & R. Wijers (Elsevier), in press (astro-ph/0402176)

Kaspi, V. M., Gavriil, F. P., Woods, P. M., Jensen, J. B., Roberts, M. S. E., & Chakrabarty, D. 2003, ApJ, 588, L93

Kern, B. & Martin, C. 2002, Nature, 415, 527

Kouveliotou, C., Dieters, S., Strohmayer, T., van Paradijs, J., Fishman, G. J., Meegan, C. A., Hurley, K., Kommers, J., Smith, I., Frail, D., & Murakami, T. 1998, Nature, 393, 235

Kouveliotou, C., Eichler, D., Woods, P. M., Lyubarsky, Y., Patel, S. K., Göğüş, E., van der Klis, M., Tennant, A., Wachter, S., & Hurley, K. 2003, ApJ, 596, L79

Manchester, R. N. & Taylor, J. H. 1977, Pulsars (San Francisco: Freeman)

Massey, P. 1997, A User's Guide to CCD Reductions with IRAF, NOAO, Tucson, Arizona

Massey, P. & Davis, L. E. 1992, A User's Guide to Stellar CCD Photometry with IRAF, NOAO, Tucson, Arizona

Mazets, E. P., Golenetskii, S. V., Il'inskii, V. N., Apetkar', R. L., & Gur'yan, Y. A. 1979, Nature, 282, 587

Özel, F. 2004, ApJ, submitted (astro-ph/0404144)

Patel, S. K., Kouveliotou, C., Woods, P. M., Tennant, A. F., Weisskopf, M. C., Finger, M. H., Göğüş, E., van der Klis, M., & Belloni, T. 2001, ApJ, 563, L45

Perna, R., Hernquist, L., & Narayan, R. 2000, ApJ, 541, 344

Predehl, P. & Schmitt, J. H. M. M. 1995, A&A, 293, 889

Rea, N., Testa, V., Israel, G. L., Mereghetti, S., Perna, R., Stella, L., Tiengo, A., Mangano, V., Oosterbroek, T., Mignani, R., Curto, G. L., Campana, S., & Covino, S. 2004, A&A, 425, L5

Stetson, P. B. 1987, PASP, 99, 191

Tam, C. R., Kaspi, V. K., van Kerkwijk, M. H., & Durant, M. 2004, ApJ, 617, L53

Tauris, T. M. & van den Heuvel, E. P. J. 2004, in Compact Stellar X-ray Sources, ed. W. H. G. Lewin & M. van der Klis (United Kingdom: Cambridge University Press), in press (astro-ph/0303456)

Thompson, C. & Duncan, R. C. 1993, ApJ, 408, 194

Thompson, C. & Duncan, R. C. 1995, MNRAS, 275, 255

Thompson, C. & Duncan, R. C. 1996, ApJ, 473, 322

Thompson, C. & Duncan, R. C. 2001, ApJ, 561, 980

Thompson, C., Duncan, R. C., Woods, P. M., Kouveliotou, C., Finger, M. H., & van Paradijs, J. 2000, ApJ, 543, 340

Thompson, C., Lyutikov, M., & Kulkarni, S. R. 2002, ApJ, 574, 332

Tokunaga, A. T., Simons, D. A., & Vacca, W. D. 2002, PASP, 114, 180

Vrtilek, S. D., Raymond, J. C., Garcia, M. R., Verbunt, F., Hasinger, G., & Kurster, M. 1990, A&A, 235, 162

Wang, Z. & Chakrabarty, D. 2002, ApJ, 579, L33

Woods, P. M., Kaspi, V. M., Thompson, C., Gavriil, F. P., Marshall, H. L., Chakrabarty, D., Flanagan, K., Heyl, J., & Hernquist, L. 2004, ApJ, 605, 378

Woods, P. M. & Thompson, C. 2004, in Compact Stellar X-ray Sources, ed. W. H. G. Lewin & M. van der Klis (United Kingdom: Cambridge University Press), in press (also available at astro-ph/0406133)